JVST A
Journal of Vacuum Science & Technology A

ARTICLE

avs.scitation.org/journal/jva

Plasma-enhanced atomic layer deposition of SiO_2 film using capacitively coupled Ar/O_2 plasmas: A computational investigation

Cite as: J. Vac. Sci. Technol. A 39, 052403 (2021); doi: 10.1116/6.0001121
Submitted: 6 May 2021 · Accepted: 8 July 2021 ·
Published Online: 3 August 2021

Chenhui Qu,[1,a)] Yukinori Sakiyama,[2,b)] Pulkit Agarwal,[2,c)] and Mark J. Kushner[1,d)]

AFFILIATIONS

[1]Department of Electrical Engineering and Computer Science, University of Michigan, 1301 Beal Ave., Ann Arbor, Michigan 48109-2122
[2]Lam Research Corporation, 11361 SW Leveton Drive, Tualatin, Oregon 97062

Note: This paper is part of the 2022 Special Topic Collection on Atomic Layer Deposition (ALD).
[a)]**Current address:** Lam Research Corporation, 4300 Cushing Pkwy, Fremont, CA 94538; **electronic mail:** chenqu@umich.edu
[b)]**Electronic mail:** Yukinori.Sakiyama@lamresearch.com
[c)]**Electronic mail:** Pulkit.Agarwal@lamresearch.com
[d)]**Author to whom correspondence should be addressed:** mjkush@umich.edu

ABSTRACT

Plasma-enhanced atomic layer deposition (PE-ALD) is widely used for dielectric deposition in semiconductor fabrication due to its ability to operate at low temperatures while having high precision control. The PE-ALD process consists of two subcycles: precursor dosing and plasma exposure with gas purging and filling in between. In the PE-ALD of SiO_2, a Si-containing precursor is first deposited on the surface, usually in a plasma-free environment. The surface is then exposed to an oxygen-containing plasma during which the residual components of the precursor are removed and the Si oxidized. Various factors affect the outcome of SiO_2 PE-ALD, such as exposure times during each step, steric hindrance of the Si precursor, and plasma properties, such as the energy of ions incident onto the film. The results from computational investigations of the first layers of SiO_2 PE-ALD at both reactor (cm) and feature (nm) scales are discussed in this paper. The example system uses bis(tertiary-butylamino)silane, $SiH_2[NH(C_4H_9)]_2$ as the silicon precursor during dosing and plasmas operating in Ar/O_2 gas mixtures during the oxidation step. Parametric studies were performed for blanket deposition, as well as deposition in trenches and vias while varying power, pressure, plasma exposure time, aspect ratio, and ligand retention in the film. The general trends show that conditions that reduce the fluence of reactive oxygen species typically decrease the O/Si ratio, increase the vacancies in the films, and decrease the order of the film. Conditions that result in higher ion fluxes having higher energies produce the same result due to sputtering. The retention of ligand groups from the precursor significantly decreased growth rates while increasing vacancies and reducing the O/Si ratio.

I. INTRODUCTION

Atomic layer deposition (ALD) is a material deposition technique enabling fine control over film quality at the angstrom scale. The ALD process for oxide dielectric films typically consists of two steps—precursor dosing that delivers the primary species (here generically referred to as a metal) to the surface followed by oxidation.[1,2] An ideal ALD process is self-limiting, meaning that the kinetics of the film growth saturates, resulting in a maximum of one monolayer of deposition per cycle.[3] Saturation of the precursor dosing results from the dosing molecule being able to chemisorb on the initial surface sites but not on already dosed sites. The dosing process naturally ends when the surface is saturated. During the oxidation step, reactions naturally terminate when remnants of the dosing molecule are removed and the metal is oxidized. The deposited films typically have high conformality and uniformity, which are necessary for applications ranging from semiconductor device manufacturing and solar panel fabrication to novel applications such as the fabrication of fuel cells.[4–9] For semiconductor

microelectronics fabrication, deposition of silicon-based dielectrics is one of the high-value ALD processes that is under active investigation with high volume manufacturing (HVM) available for certain applications.[10–16]

Thin SiO_2 films are widely used as isolation liners and sidewall spacers in microelectronic devices.[17–19] Although sophisticated film deposition approaches are already in HVM, the sub-10 nm technology nodes have challenging demands for high-conformality film deposition. Also, three-dimensional NAND memory applications require conformal deposition in high aspect ratio features in non-line-of-site locations. One of the most pressing issues challenging deposition of thin SiO_2 films is the ability to engineer film properties in high aspect ratio (HAR) structures for a variety of applications that may require a precise tuning of film's electrical, mechanical, and optical properties. The presence of vacancies is also a major concern that can lead to critical issues such as electrical breakdown.[20,21] Stathis reported that in films thinner than 2 nm, a single vacancy is enough to produce electrical breakdown.[21]

Thermal ALD is one of the well-established SiO_2 film deposition techniques. Typically, in a thermal ALD process, the target surface is sequentially treated with inorganic silicon precursors [e.g., $SiCl_4$, $SiCl_3H$, and DIPAS ($H_3Si[N\{(CH)(CH_3)_2\}]$] and oxidants (e.g., H_2O and O_3). Each cycle produces a fraction of a monolayer of film. Repeating these steps builds the film layer by layer. To activate these processes, the substrate is usually heated to >300 °C. Using a $SiCl_4$ and H_2O binary reaction sequence, Sneh *et al.* achieved controlled SiO_2 film deposition at temperatures of 330–410 °C at a growth rate of 0.11 nm/cycle.[22] In a later work, Lee *et al.* proposed a SiO_2 ALD mechanism having cycles of alternating Si_2Cl_6 and O_3 with a substrate temperature of 403–453 °C.[23] In this work, a temperature of 471 °C or higher was needed for a deposition rate higher than 0.32 nm/cycle. Even though this temperature is already lower than that used in many other SiO_2 deposition techniques, such as low-pressure chemical vapor deposition, it is still high enough to tax the allowed thermal budget of the fabrication process. This high temperature also limits the use of temperature-sensitive materials such as those used for flexible electronics. Alternate low-temperature techniques are needed.

One way to decrease the required temperature for ALD of SiO_2 is to use plasma-enhanced ALD (PE-ALD). In a typical SiO_2 PE-ALD process, the target surface is first treated with the silicon precursor, which is then followed by oxidation in an oxygen-containing plasma. The process is repeated, and SiO_2 is, thus, grown layer by layer. Unlike thermal ALD, in PE-ALD oxidation, reactions are enabled by reactive species in the plasma that require significantly lower substrate temperatures. Fang *et al.* reported that $O_2(^1\Delta)$, O_3, and $O(^1D)$ are the primary reactants that oxidize a precursor-dosed surface during plasma exposures for SiO_2 PE-ALD, which then enables the low-temperature deposition.[24] Choi *et al.* reported on deposition of SiO_2 films of tens of nanometer thickness using PE-ALD at temperatures of less than 200 °C.[25] Jeon *et al.* used plasma-activated triisopropylsilane [(iPr)3SiH] as a silicon precursor during dosing in a PE-ALD process.[15] They found that the deposition temperature can be decreased to as low as 50 °C and that the SiO_2 films had no detectable impurities.

In a side-by-side comparison of SiO_2 films deposited using PE-ALD and plasma-enhanced chemical vapor deposition (PECVD), Jung *et al.* found that the PE-ALD prepared film had fewer impurities, more proper stoichiometry, and lower leakage current.[16] When tested as the gate insulator in a thin film transistor, PE-ALD SiO_2 films appeared to be less susceptible to negative threshold voltage shift than PECVD films due to a smoother insulator/channel contact interface. Civale *et al.* investigated 200 nm-thick SiO_2 liners for a high aspect ratio (25:1) through silicon vias as used in a 3D interconnect prepared using PE-ALD.[17] They reported near-ideal film conformality and electrical properties, suggesting a possible role of PE-ALD grown SiO_2 films in HAR applications. However, the quality of SiO_2 films grown using PE-ALD is sensitive to the scale of the feature. For example, the quality of the film deposited on the sidewall of a feature varies significantly with respect to the aspect ratio. It is, therefore, challenging to obtain uniform, high-quality films throughout a HAR feature.

Similar to other thin film deposition techniques, many parameters can affect the quality of the film prepared using PE-ALD. Shin *et al.* found that when using DIPAS [di-isopropylaminosilane, $SiH_3N(C_3H_7)_2$] as the silicon precursor at 50 °C, the deposition rate measured as growth per cycle (GPC) depended on the plasma exposure time.[12] The GPC decreased from 0.2 to 0.16 nm/cycle as the O_2 plasma exposure time increased from 0.5 to 5.0 s. The causes of this decrease were suggested to be substrate heating and film densification. Kobayashi *et al.* found that in some cases, a higher GPC can be achieved with a lower deposition temperature.[10] Using BDEAS (bis(diethylamino)silane, $SiH_2[N(CH_2CH_3)_2]_2$) as the silicon precursor and an O_2 plasma as the oxidant, they found that the saturated GPC increased from 0.10 to 0.15 nm/cycle as the deposition temperature decreased from 300 to 50 °C. They concluded that as the substrate temperature increases, desorption reactions decrease the GPC.

In addition to the operating conditions, the chemical properties of silicon precursors also have a significant impact on the PE-ALD process.[26,27] In work comparing SiO_2 PE-ALD by silicon precursors, BTBAS (bis(tertiary-butylamino)silane, $SiH_2[NH(C_4H_9)]_2$), BDEAS, and DSBAS (di-*sec*-butylaminosilane, $SiH_3[N(C_4H_9)_2]$), Mallikarjunan *et al.* found that because DSBAS is a monoaminosilane precursor, it has fewer organic substitutions than BTBAS and BDEAS.[27] Therefore, the surface packing density of silicon-containing components after the precursor dosing is higher when using DSBAS, and so the growth rate is higher. This is an example of steric hindrance—blocking of surface sites due to the size of the chemisorbed precursor molecule. Using density functional theory, Murray *et al.* concluded that ligand groups first formed bound reactant structures with the surface, which initiated the precursor adsorption, and had an impact on further surface reaction probabilities.[11] However, if these large ligand groups fail to desorb from the surface, they can result in significant steric hindrance and impede further deposition. Steric hindrance occurs when the ligand group from the silicon precursor remains on the target surface and blocks the otherwise exposed neighboring surfaces. The blockage reduces the surface coverage of the desired species and hinders the growth of the film.

In this paper, we discuss results from computational investigations of the PE-ALD of SiO_2 films for blanket deposition and deposition in trenches and vias. Emphasis is on the consequences of

steric factors and codeposition probabilities of the ligand groups of the Si precursor molecules. The results from the parametric studies of power (400–1000 W), pressure (0.5–2 Torr), and exposure time (0.2–2 s) during the oxidation step will be discussed. Changing power was found to be less effective in terms of improving film stoichiometry when compared with increasing pressure for the parameter space investigated. Increasing plasma exposure time yields denser and more uniform films. The codeposition probability of the ligand group of the silicon precursor affects film growth rate and density, both decreasing with an increase in the ligand codeposition probability.

The models used in this investigation are briefly discussed in Sec. II. The deposition mechanism and surface reactions are presented in Sec. III. Plasma and film properties as a function of power, pressure, ligand group codeposition probability, plasma exposure time, and feature aspect ratio are discussed in Sec. IV. Concluding remarks are presented in Sec. V.

II. DESCRIPTION OF THE MODEL

The computational platforms used in this work are the Hybrid Plasma Equipment Model (HPEM) for the reactor scale simulations and the Monte Carlo Feature Profile Model (MCFPM) for the feature scale. The HPEM performs reactor scale simulations for plasma properties, generating fluxes and energy and angular distributions (EADs) of reactive species to the substrate. These fluxes and distributions are then used in the MCFPM for feature scale simulation. Details of the models are discussed in Ref. 28 for the HPEM and Refs. 29 and 30 for the MCFPM. Only brief descriptions are provided here.

The HPEM is a 2D hydrodynamic model resolving plasma phenomena through a time-slicing approach. Different plasma phenomena are addressed by different modules that exchange information on time scales that vary with discharge conditions. The modules that were used in this work are the Fluid Kinetics-Poisson Module (FKPM), the Electron Energy Transport Module (EETM), and the Plasma Chemistry Monte Carlo Module (PCMCM). In the FKPM, the continuity, momentum, and energy equations of the heavy particles are solved coincidently with Poisson's equation to provide heavy particle densities, fluxes and temperatures, and electrostatic potential. Electron fluxes are given by a drift-diffusion formulation with automatic upwind–downwind capabilities. An electron energy equation provides the electron temperature with electron impact and rate coefficients provided by stationary solutions of Boltzmann's equation for the electron energy distribution. Secondary electrons emitted from surfaces by ion bombardment (beam electrons) are tracked in the EETM using Monte Carlo techniques. The EADs of ions and neutrals to the substrate are produced in the PCMCM using a Monte Carlo simulation.

The MCFPM is a voxel-based simulator used to investigate topological evolution of nanoscale features. In the MCFPM, gas-phase pseudoparticles with EADs provided by the HPEM are launched toward the surface from above the feature and tracked using the Monte Carlo technique until colliding with a solid material. The nm-scale feature is resolved using cubic voxels. Each voxel is assigned material properties. For each unique surface material, a reaction mechanism is specified for collisions with all gas-phase species. The reaction mechanism includes the parameters required to compute the corresponding reaction probabilities (e.g., energy threshold and angular dependence). When a gas-phase pseudoparticle collides with a solid material cell, the cumulative reaction probabilities of processes between the gas-phase species and the material are computed and normalized to unity. A random number is then used to choose the process that occurs. When a deposition occurs, additional voxels representing the deposited materials are added to the site of the collision. When sputtering occurs, the voxel that represents the solid material at the colliding site is removed from the mesh as a gas-phase reaction product.

The energy-dependent reaction probability (e.g., sputtering) used in the model has the form of

$$p(E_i, \theta) = p_0 \left(\frac{E_i - E_{th}}{E_r - E_{th}}\right)^n f(\theta), \tag{1}$$

where E_i is the energy of the incident gas-phase particle, E_r is a reference energy, E_{th} is the threshold energy, and θ is the incident angle.[31,32] The exponential term n is 0.5 for the energy-dependent reactions discussed in this paper. For physical sputtering by energetic ions, $f(\theta)$ is maximum at 60°, gradually decreasing to zero at the grazing angle, with a nonzero value at normal incidence.

Collisions between gas-phase particles are included in the MCFPM. These processes can be important when the pressure is high (several Torr) and when the feature has a HAR. Collisions between gas-phase species can broaden their angular distribution deep in a high aspect ratio feature. Collisions between gas-phase species randomly occur with the averaged mean free path between collisions being a function of gas composition and pressure. Here, all gas-phase collisions are purely elastic with isotropic scattering.

In deposition in HAR features, energetic particles may collide with sidewalls several times before reaching the bottom of the feature. During these collisions, particles lose some of their energy to the surface. A gas-phase particle with energy E_i striking a surface with an incident angle of θ retains the energy of E_s after surface reflection,

$$E_s(\theta) = E_i \left(\frac{E_i - E_c}{E_{ts} - E_c}\right) \left(\frac{\theta - \theta_c}{90° - \theta_c}\right), \tag{2}$$

where E_{ts} is the threshold energy for specular scattering, E_c is the cut-off energy for diffusive scattering, and θ_c is the lower angular boundary for specular scattering. Particles with $E_i > E_{ts}$ preserve all the energy, and particles with $E_i < E_c$, or $\theta < \theta_c$ are diffusively scattered. In this study, $E_{ts} = 50$ eV, $E_c = 0$, and $\theta_c = 60°$.

Gas-phase species adsorbing on surfaces thermally diffuse along the surface prior to chemisorption. The transport algorithm randomly chooses directions in which the adsorbed species diffuses based on activation energy barriers that are dependent on the local topology.

The steric hindrance resulting from large ligand groups contained in the Si precursor is addressed by "codepositing" a voxel representing a ligand next to the voxel where the primarily silicon is deposited. The gas-phase Si precursor is specified to have N ligand groups. A codeposition probability p_R is assigned to each

ligand group. Upon deposition of the Si precursor, a random number $r = (0,1)$ is selected. If $r \leq p_R$, then a codeposition of the first ligand is attempted. A search is made of the sites surrounding the deposition site for an empty voxel to codeposit the ligand. The search order is randomized. For a 2D simulation, there are eight possible sites. For a 3D simulation, there are 26 possible sites. When an empty site is found, a ligand is placed at that site. The process is then repeated for the N ligand groups.

The species included in the reactor scale simulation are Ar, Ar($1s_5$), Ar($1s_4$), Ar($1s_3$), Ar($1s_2$), Ar(4p), Ar(4d), Ar_2^*, Ar^+, Ar_2^+, O_2, O_2(v), $O_2(a^1\Delta_g)$, $O_2(b^1\Sigma_g^+)$, O_2^+, O_2^-, $O(^1D)$, $O(3s\ ^5S^0)$, $O(3s\ ^3S^0)$, $O(3p\ ^5P)$, $O(^1S)$, O^+, O^-, O_3, O_3^-, and electrons. The reaction mechanism for the Ar/O_2 plasma is the same as discussed in Ref. 30.

III. SURFACE REACTION MECHANISM FOR SiO_2 PE-ALD USING Ar/O_2 PLASMA

The gas-phase species, surface sites, and surface reaction mechanism for SiO_2 PE-ALD using a silicon precursor with two ligand groups (such as BTBAS) and Ar/O_2 plasma oxidation are shown in the Appendix. Surface species are denoted by "(s)."

The gas-phase species included in the feature scale simulation can be classified as (a) ions bringing high energy into the feature due to acceleration in the sheath, (b) hot neutrals having similar energies as ions, produced when ions strike a surface, lose their charge, and reflect from the wall, (c) thermal neutrals have energy less than 0.1 eV. Thermal neutrals, such as O and O_3, are the primary species for surface oxidation. A final type of gas phase species is (d) reaction products, being gas-phase particles removed from the surface by ions and hot neutrals or chemical reactions. Reaction products can be redeposited on the surface.

Surface sites in the model are classified by the layer they belong to. A silicon layer contains sites produced from precursor dosing. An oxygen layer consists of sites produced during plasma exposure. Each voxel in the MCFPM representing a site in the oxygen layer ideally contains two physical bonds for a perfectly stoichiometric SiO_2 film. For example, x–Si–y(s) species denotes x and y sites connected to a shared silicon atom, although this silicon atom is not included in that voxel.

The PE-ALD process starts with a precursor dosing a surface covered with hydroxyl sites. The ligand group R from the precursor SiH_2R_2 containing two ligand groups combines with the hydrogen from a hydroxyl site and forms a volatile gas-phase species HR. The remaining precursor SiH_2 is then bonded to the oxygen and deposited on the surface as SiH_2(s). In a process that fully eliminates the ligands,

$$\mathrm{OH-Si-OH(s)} + \mathrm{SiH_2R_2} \rightarrow \mathrm{O_2(s)} + \mathrm{SiH_2(s)} + 2\mathrm{HR}. \quad (3)$$

In ideal PE-ALD, the surface is saturated with OH–Si–OH(s) at the beginning of the precursor step. From a practical matter, there needs to be a first layer on the substrate to start the PE-ALD process. For startup purposes, the underlying material is represented as W(s) in the mechanism, a surface species that undergoes the same reaction as in Eq. (3).

In addition to the ideal, one-step passivation process in Eq. (3), there are cases where deposition of SiH_2(s) occurs at surface sites having insufficient hydroxyls to completely remove the ligands and produce stoichiometric bonding. For example,

$$\mathrm{OH-Si-H(s)} + \mathrm{SiH_2R_2} \rightarrow \mathrm{O(s)} + \mathrm{SiH_2(s)} + 2\mathrm{HR}, \quad (4a)$$

$$\mathrm{OH-Si(s)} + \mathrm{SiH_2R_2} \rightarrow \mathrm{O(s)} + \mathrm{SiH_2(s)} + p_R\mathrm{R(s)} + (1-p_R)\mathrm{HR} + \mathrm{HR}, \quad (4b)$$

$$\mathrm{O-Si-H(s)} + \mathrm{SiH_2R_2} \rightarrow \mathrm{O(s)} + \mathrm{SiH_2(s)} + p_R\mathrm{R(s)} + (1-p_R)\mathrm{HR} + \mathrm{HR}, \quad (4c)$$

$$\mathrm{OH-Si-O(s)} + \mathrm{SiH_2R_2} \rightarrow \mathrm{O_2(s)} + \mathrm{SiH_2(s)} + p_R\mathrm{R(s)} + (1-p_R)\mathrm{HR} + \mathrm{HR}. \quad (4d)$$

In reactions (4a)–(4c), O(s) instead of O_2(s) is produced. If this happens too frequently, the O/Si ratio will decrease, leading to a nonstoichiometric film. Note that ligand groups R(s) are not definitively codeposited with SiH_2(s) even when the direct surface site has insufficient hydroxyl sites, such as in reactions (4b)–(4d). In these instances, if the nearest neighbors of the direct surface site can provide hydrogen atoms, the ligand from the silicon precursor can combine with them and form a volatile HR. That said, it would be very computationally expensive to check the nearby neighbors of a direct surface site wherever a deposition occurs. Therefore, we rely on the codeposition probability, p_R, for the deposition of ligand remnants R(s). If a SiH_2(s) is deposited on a surface with SiH_2R_2 as a reactant, an R(s) site is codeposited with the probability p_R.

During plasma exposure, the surface is oxidized by reactive oxygen species (ROS) from the plasma. The goal of plasma exposure is to deposit the oxygen layer on the film and populate the surface with hydroxyl sites. The oxidation can be a multistep process,

$$\mathrm{SiH_2(s)} + \mathrm{O} \rightarrow \mathrm{Si(s)} + \mathrm{OH-Si-H(s)}, \quad (5a)$$

$$\mathrm{OH-Si-H(s)} + \mathrm{O} \rightarrow \mathrm{OH-Si-OH(s)}. \quad (5b)$$

Both excited state oxygen radicals [such as $O(^1D)$] and O^+ can produce the same reactions though with a higher probability due to their higher internal energy. The oxidation can also be a one-step process by excited state oxygen molecules,

$$\mathrm{SiH_2(s)} + \mathrm{O_2^*} \rightarrow \mathrm{Si(s)} + \mathrm{OH-Si-OH(s)}. \quad (6)$$

In spite of the plasma typically operating at pressures of up to a few Torr, some ions (or hot neutrals) reach the surface with energy exceeding tens of electron volts (eV). These particles can produce damage by sputtering,

$$\mathrm{OH-Si-OH(s)} + \mathrm{I^+} \rightarrow \mathrm{OH-Si(s)} + \mathrm{OH} + \mathrm{I(h)}, \quad (7a)$$

$$\mathrm{SiH_2(s)} + \mathrm{I^+} \rightarrow \mathrm{SiH_2} + \mathrm{I(h)}, \quad (7b)$$

$$\mathrm{R(s)} + \mathrm{I^+} \rightarrow \mathrm{R} + \mathrm{I(h)}, \quad (7c)$$

where I^+ is an ion and I(h) denotes a hot neutral. (Hot neutrals undergo the same reactions as ions.) In this work, the sputtering thresholds for oxygen and hydroxyl are 30 eV, and for silicon, SiH_2(s) and SiH(s) are 35 eV. The sputtered particles can be redeposited on the surface when they strike sites having dangling bonds. For example,

$$SiH(s) + SiH_2 \rightarrow SiH(s) + SiH_2(s), \quad (8a)$$

$$SiH(s) + Si \rightarrow SiH(s) + Si(s), \quad (8b)$$

$$O(s) + SiH_2 \rightarrow O(s) + SiH_2(s). \quad (8c)$$

These reactions can introduce disorder and imperfections in the film.

Other than redeposition on a surface, gas-phase OH and R groups can abstract hydrogen and create a dangling bond on the surface:

$$SiH_2(s) + OH \rightarrow SiH(s) + H_2O, \quad (9a)$$

$$OH - Si - OH(s) + OH \rightarrow OH - Si - O(s) + H_2O, \quad (9b)$$

$$SiH_2(s) + R \rightarrow SiH(s) + HR, \quad (9c)$$

$$OH - Si - OH(s) + R \rightarrow OH - Si - O(s) + HR. \quad (9d)$$

Hydrogen bonds to Si or O. Sputtering of only H atoms was not included in the mechanism due to the low kinetic energy transfer efficiency between a light hydrogen atom and a heavy incident particle.

In addition to sputtering, recombination–abstraction reactions of oxygen radicals and O_3 can also reduce the oxygen content of SiO_2 films,

$$O(s) + O \rightarrow O_2, \quad (10a)$$

$$O_2(s) + O \rightarrow O(s) + O_2, \quad (10b)$$

$$O(s) + O_3 \rightarrow O_2 + O_2. \quad (10c)$$

However, in this work, these reactions have low reaction probabilities ($p_0 = 6 \times 10^{-5}$) due to the low substrate temperature.[33]

Removal of the R(s) ligands can occur through two processes. The first is the sputtering of R(s) by ions and hot neutrals. The second is through replacement reactions of R(s) with ROS where O breaks the Si–R(s) bond and replaces R(s),[34]

$$R(s) + O \rightarrow O(s) + R, \quad (11a)$$

$$R(s) + O^* \rightarrow O(s) + R, \quad (11b)$$

$$R(s) + O_3 \rightarrow O(s) + R + O_2. \quad (11c)$$

At low substrate temperatures, these reactions have low reaction probabilities. In experiments by Lu *et al.*,[34] the oxygen plasma exposure time to remove the ligands was up to several minutes, which is much longer than the exposure time of any given cycle (<2 s) addressed here.

Upon striking a surface, excited state gas-phase particles can be quenched to the ground state or undergo dissociation,

$$Surface(s) + O_3 \rightarrow Surface(s) + O + O_2, \quad (12a)$$

$$Surface(s) + O^* \rightarrow Surface(s) + O, \quad (12b)$$

$$Surface(s) + O_2^* \rightarrow Surface(s) + O_2. \quad (12c)$$

These processes have significant impact on fluxes of reactive species to the bottom of HAR features.

IV. PLASMA CHARACTERISTICS AND FILM DEPOSITION PROFILE

A schematic of the reactor used in this work is in Fig. 1. The system is a cylindrically symmetric capacitively coupled plasma (CCP) reactor designed to process a 30 cm diameter wafer. The wafer is placed on a grounded substrate surrounded by a quartz (dielectric constant $\varepsilon_r = 4.0$) focus ring. The top electrode, 1.5 cm above the substrate, is powered at 10 MHz through a blocking capacitor upon which a DC bias is generated. The primary showerhead coincides with the top electrode and injects an $Ar/O_2 = 80/20$ gas mixture at 5 standard liters per minute (slm). The secondary electron emission coefficient for ions is 0.05 for all the surfaces exposed to the plasma. In the base case, pressure in the reactor is held constant at 2 Torr by varying the flow rate through the pump, and the input power is 500 W, obtained by varying the voltage applied to the top electrode. The substrate and focus ring temperatures are held constant at 50 °C. The temperatures of all other surfaces are held constant at 25 °C.

The base case conditions produce a time-averaged plasma potential of 137 V. The DC bias is −30 V on the blocking capacitor

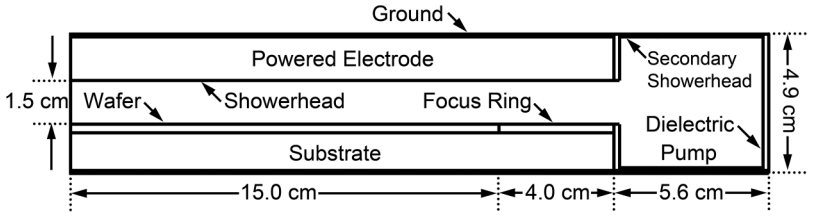

FIG. 1. Geometry of the reactor. The base case conditions are 500 W at 10 MHz applied to the top electrode. The 2 Torr pressure is maintained by a 5 slm flow of $Ar/O_2 = 4/1$ through the primary gas inlet.

connected to the top electrode. The dominant cations and anions are O_2^+ and O^-. The O_2 flow, electron density (n_e), O_2^+ density, and O^- density are shown in Fig. 2. The plasma properties are predominantly determined by the gas flow from the primary showerhead. The electron density n_e peaks at $r = 19$ cm at 2.3×10^{10} cm^{-3} due to electric field enhancement at the edge of the top electrode but is otherwise uniform in the radial direction across the wafer with a value of 1.0×10^{10} cm^{-3}. The electronegativity [(negative ion density)/(positive ion density)] is about 30%. The wafer has a fairly high conductivity (σ) of 0.05 Ω^{-1} cm^{-1}, while the quartz focus ring is an ideal dielectric. When solving Poisson's equation using the substrate as a ground, the electric field is negligible in the wafer but relatively high in the focus ring (150 V/cm). The end result is a higher potential on the surface of the focus ring (50 V) than on the wafer (4 V), which perturbs the sheath on the wafer–quartz interface and causes a nonuniform plasma distribution above the focus ring. However, both the maximum in n_e and this perturbation of the plasma distribution occur downstream of the gas flow. Therefore, their impacts on the bulk plasma and fluxes to the wafer are insignificant.

In such a high pressure CCP, ionization is sustained by bulk electrons, which are mostly resistively heated, and beam electrons that originate from secondary electron emission. At 2 Torr, the electron mean free path is much smaller than the gap length. Therefore, it is difficult for bulk electrons heated at the edge of the sheath to transport to midgap with enough energy to enable further ionization. Sheath accelerated secondary electrons can have energy from tens of electron volts to 100 eV, enabling them to

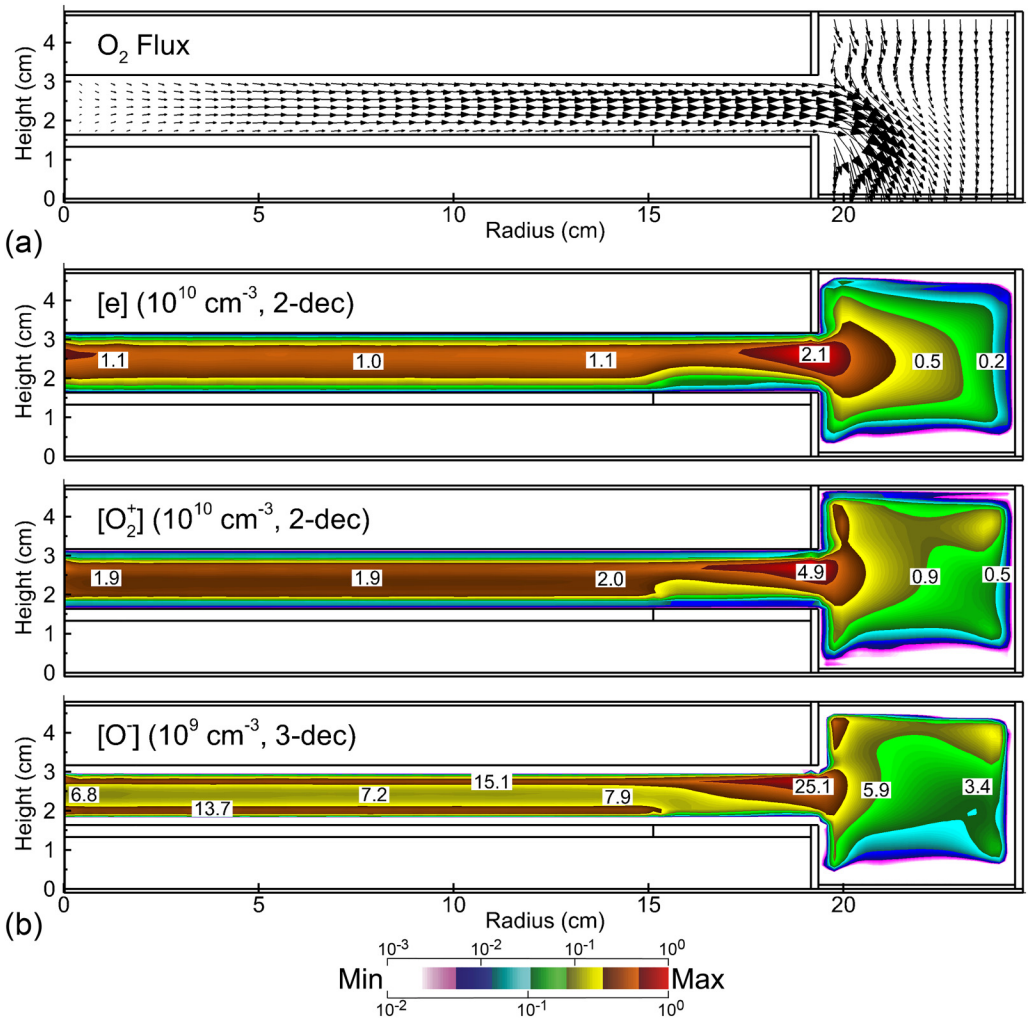

FIG. 2. Plasma properties during the oxidation step for the base case conditions (500 W, 10 MHz, 2 Torr, $Ar/O_2 = 4/1$ at 5 slm). (a) O_2 flux with the length of the vectors showing relative values. (b) Densities of electrons, O_2^+ and O^-. Contours are plotted on a log scale over the indicated range. The contours are labeled with the units noted in each image.

travel further into the bulk plasma. The ionization source for bulk electrons (S_e) near the sheath is comparable with that for beam electrons (S_{eb}) with $S_e = 6.7 \times 10^{15}\,\mathrm{cm^{-3}\,s^{-1}}$ and $S_{eb} = 4.4 \times 10^{15}\,\mathrm{cm^{-3}\,s^{-1}}$. However, at 0.3 cm below the top electrode, S_e drops to near zero, and the ionization is maintained by secondary electrons ($S_{eb} = 2.7 \times 10^{15}\,\mathrm{cm^{-3}\,s^{-1}}$). With the plasma mainly sustained by beam electrons, the plasma operates in the γ-mode.

The dominant cation O_2^+ shares the same uniform radial distribution across the wafer as electrons with a density of 1.9–2 $\times 10^{10}\,\mathrm{cm^{-3}}$. O_2 undergoes dissociative attachment producing O^-, which has a relatively high density. The O^- density is nearly 70% that of n_e in the bulk plasma. However, because of its low temperature, O^- is confined in the bulk plasma and has a negligible flux to the wafer.

The EADs onto the wafer of Ar^+, O_2^+, and O are shown in Fig. 3(a). These data are averaged over the wafer and averaged in angle across the normal. Both Ar^+ and O_2^+ have relatively narrow angular distributions with an incident angle of less than 20°. The sheath above the wafer accelerates ions up to 45 eV. However, the plasma potential is 137 V, almost three times the peak ion energy, indicating that the sheath is highly collisional. Ions dissipate their energy through multiple collisions as they travel across the sheath. Since the majority of ions have energy less than 20 eV, lower than the sputtering thresholds (30 eV), only minor ion bombardment damage to the film is expected. Neutral species have close to thermal energy and a wide angular distribution. The peak O energy reaches 0.3 eV, which is likely caused by charge exchange reactions near the wafer surface. When hot O^+ collide with O, they exchange the charge but preserve their initial kinetic energy and form a hot O atom and a cold O^+. The hot neutral will no longer gain energy from the electric field and will lose its energy through collisions with other particles as it moves toward the wafer. Consequently, when the hot O atom strikes the surface, its energy is much lower than the energy of most ions but is still higher than the thermal energy of most neutral species. This higher energy of up to 0.3 eV is unlikely to cause any significant difference regarding the surface reaction rates.

The fluxes of major species onto the wafer as a function of radius are shown in Fig. 3(b). Most species have a fairly uniform flux across the wafer with any noise being due to statistical fluctuations resulting from the finite number of particles used in the electron Monte Carlo Simulation for tracking secondary electrons. For example, the O flux is uniform at $1.6 \times 10^{18}\,\mathrm{cm^{-2}\,s^{-1}}$ at $r < 12$ cm with only minor fluctuation ($\pm 1.0 \times 10^{16}\,\mathrm{cm^{-2}\,s^{-1}}$). The flux increases by about 5% at the edge of the wafer due to a slight increase of O density near the edge of the top electrode. Note that the high pressure produces a reasonably large density of O_3 ($3.6 \times 10^{11}\,\mathrm{cm^{-3}}$ at midgap), which produces a O_3 flux of $\approx 3 \times 10^{15}\,\mathrm{cm^{-3}\,s^{-1}}$. Even though it is three orders of magnitude smaller than the O flux, O_3 is an important oxidant that is commonly used in the deposition of oxides due to its highly reactive nature. The dominant cations Ar^+ and O_2^+ also have fluxes of $\sim 10^{15}\,\mathrm{cm^{-2}\,s^{-1}}$. Even though the resulting sputtering is not expected to be severe for the base case, changing the operating conditions such as decreasing the pressure can increase ion energy and enter a damaging regime.

A schematic of the computational PE-ALD process for a SiO_2 film is shown in Fig. 4. The substrate is repeatedly and sequentially

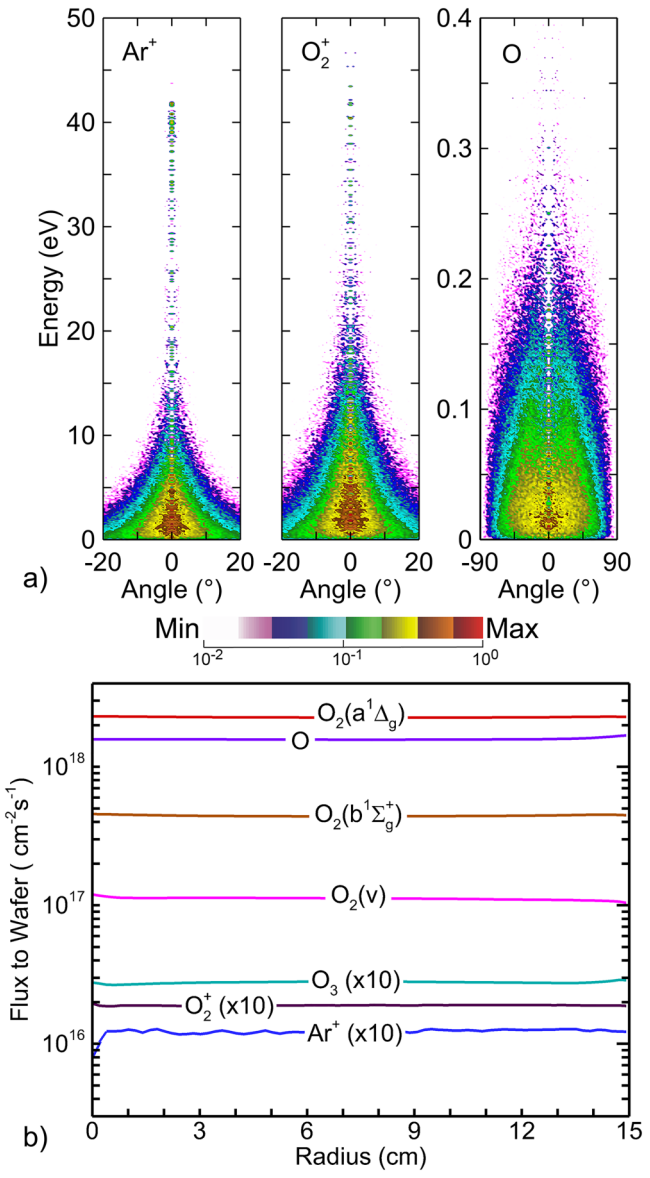

FIG. 3. Plasma properties during the oxidation step for the base case conditions (500 W, 10 MHz, 2 Torr, Ar/O_2 = 4/1 at 5 slm). (a) EADs for Ar^+, O_2^+, and O atoms. (b) Fluxes of reactants to the wafer. The noise in the flux of Ar^+ is a result of the statistics of the Monte Carlo simulation used for secondary electrons.

exposed to the silicon precursor and Ar/O_2 plasma. The gas purge between steps is not included in the simulation and we assume that no gas remains in the chamber from the previous steps. The cubic voxels used in the MCFPM are $0.5^3\,\mathrm{nm^3}$. For ideal PE-ALD with saturated and unity coverage for each step, each cycle deposits two layers of voxels representing a monolayer of silicon dioxide. The Si voxels resulting from alternating precursor dosing steps are

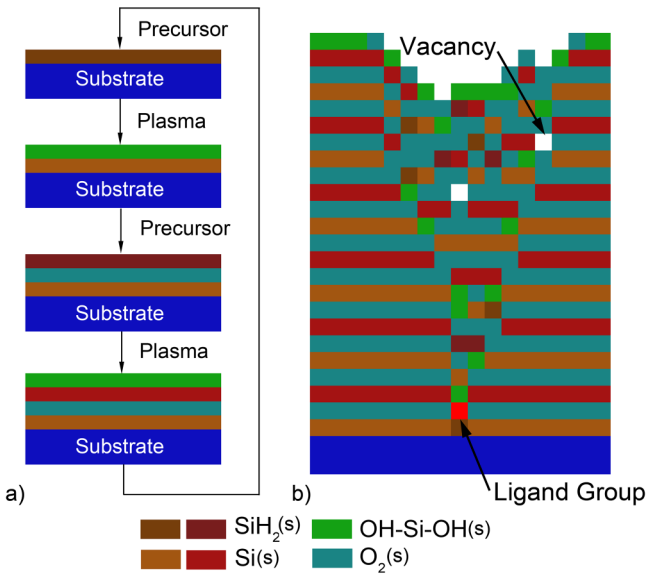

FIG. 4. Conceptual PE-ALD deposition process and outcome. (a) Flowchart of the SiO_2 PE-ALD process with alternate layers of Si color coded differently to assess the orderliness of the deposition. (b) Simulated film demonstrating the impact of ligand remnant on the subsequent layers of SiO_2 film deposition.

displayed with different colors to distinguish the Si that originates from different cycles. Perfect, saturated ALD on a flat surface would then be represented by layers of alternating colored Si sites interspersed by O_2 sites indicating conformal, stoichiometric SiO_2. Deviations from that pattern indicate some form of nonideal ALD or defects. As shown in Fig. 4(b), this nonideality or defects could result from, for example, a buried ligand group that was not removed following codeposition, OH groups that did not react with the precursor, or a vacancy due to blockage of a surface site.

Although SiO_2 is usually an amorphous material, perfect ALD would imply some sense of ordering of the film, at least structurally. The outcomes of these nonideal features and defects introduce disorder to the implied layering, slower growth rates, roughness, and porosity. The initial disruption of the layered structure caused by the embedded ligand group escalates to misalign the upper layers and produces an increasingly coarse surface. A vacancy occurs when deposition and growth of neighboring sites bridge over an unoccupied site. (A vacancy is defined as a gas-phase voxel with less than two consecutive gas voxel neighbors in any direction.) The vacancy density reduces the quality of a film that translates to a higher wet-etch rate.

In the base case, the precursor dosing time is 0.8 s, and the plasma exposure time is 1 s. During dosing, a precursor flux of $1 \times 10^{20}\ cm^{-2}\ s^{-1}$ is launched from the top of the computational domain with an isotropic angular distribution and thermal speeds. During plasma exposure, the fluxes of radicals and ions are obtained from the EADs provided by the HPEM. Unless otherwise specified, the ligand group codeposition probability $p_R = 0.005$. These conditions were chosen so that with zero codeposition probability, perfect PE-ALD would occur.

Blanket film deposition was first performed on a 65 nm (L) × 10 nm (W) area, meshed with 130 × 20 computational voxels. A reflective boundary condition was used on all the boundaries. A gas-phase particle crossing the boundary is specularly reflected back into the computational domain. The SiO_2 film deposited after 10 PE-ALD cycles is shown in Fig. 5. (Recall that every two-shaded layers of Si and O represents one monolayer of SiO_2.) The film is fairly dense (meaning lacking vacancies) and uniform for the first five cycles, becoming less ordered later in the deposition. Early in the deposition, misalignments leading to disordering that are caused by ligand remnants affect only their nearest neighbors. For a single buried ligand site, the immediate next layer will have a defect resulting from oxygen atoms being unable to reach the site underlying the ligand group. With a low codeposition probability ($p_R = 0.005$), the impact of these imperfections is reasonably small. By the end of the fifth cycle, defects are only sparsely distributed on the surface such that the film might still be considered smooth. However, these ligand-produced defects and disordering are imprinted in the vertical direction as a lower growth rate and spread in the lateral direction as reactants in successive PE-ALD cycles are blocked from adjacent sites.

With significant ligand codeposition probability, the likelihood for defect formation will also likely increase with film thickness. The thicker the film, the larger the fluence of reactants onto the surface and so the higher the likelihood that a codeposition will have

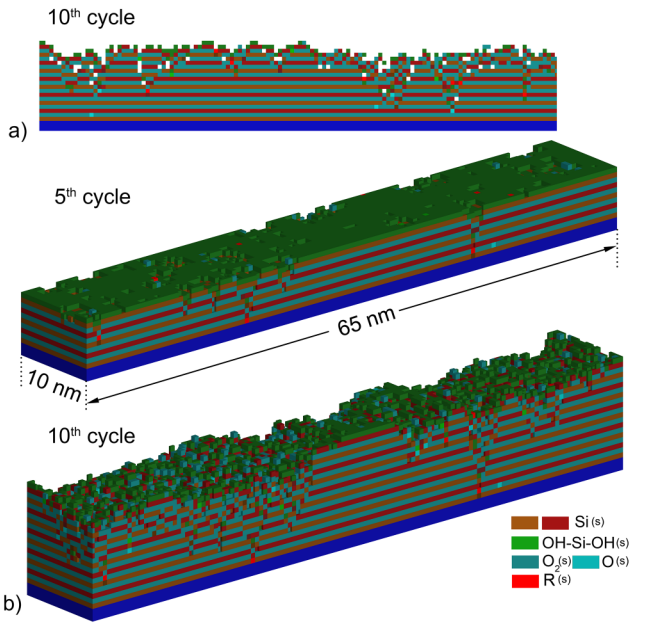

FIG. 5. PE-ALD grown SiO_2 blanket films for the base case conditions. (a) Two-dimensional slice through the middle of the film after the 10th cycle. (b) Three-dimensional profile of the film at the end of the fifth and tenth cycles.

occurred. Once that codeposition occurs, disorderliness due to the perturbing ligands and their steric hindrance spreads vertically and laterally, producing roughness in the film. In simulations for films of up to 30 layers (not shown here), finite codeposition and nonsaturated recipes do lead to rougher films. However, smooth, thick films are predicted for minor amounts of codeposition and saturated processes.

The exposure of the side of a site enables nonepitaxial deposition. For example, if the side of an OH–Si–OH(s) site faces a vacancy after plasma exposure, during the following precursor dosing, a SiH_2(s) site can deposit laterally adjacent to the OH–Si–OH(s) instead of above it. This results in a silicon atom embedded in the oxygen layer, which would have resulted from perfect PE-ALD. In this reaction, the original OH–Si–OH(s) site becomes a O_2(s) site that cannot react with the precursor during the next cycle. The site lacks the –OH(s) required to react with the ligand group from the precursor SiH_2R_2. In this case, an exposed O_2(s) locally inhibits growth. As a result, a single missing OH–Si–OH(s) induces two potential defects: a SiH_2(s) embedded in an oxygen layer and an exposed O_2(s). Both lead to locally depressed growth rates and disorderliness. The embedded SiH_2(s) at the end of plasma exposure will inhibit chemisorption of the precursor, while its neighboring OH–Si–OH(s) are uninhibited to the chemisorption. This staggered deposition may expose more sites with open sides and consequently enlarging disordered volumes.

The silicon precursor cannot directly chemisorb on the O_2(s) site to produce the Si–O bonding. Therefore, the fractional O_2(s) surface coverage increases through the deposition process, as shown in Fig. 6(a). The surface coverage ratio of O_2(s) is the fraction of surface sites that are occupied by O_2(s). The sampled area is $10 \times 10\ nm^2$ in the center of the film. The surface coverage of O_2(s) does not reach saturation in ten cycles. However, the surface coverage of O_2(s) eventually reaches a maximum of ≈40% later as the film continuously grows. The mechanism for removing exposed O_2(s) is through recombination reactions with gas-phase species, such as O, OH, and O_3, and through sputtering by energetic particles.

The accumulation of O_2(s) on the surface is in part responsible for a decreasing film growth rate with film thickness. The concentrations of O (η_O), Si (η_{Si}), vacancies (η_{Vac}), and ligand groups (η_R) in the entire film are shown in Fig. 6(b). Note that hydrogen is not counted so that $\eta_{Si} + \eta_O + \eta_{Vac} + \eta_R = 1$. In the first ten cycles (18 s excluding gas purge and refill times), both η_{Si} and η_O are relatively stable with $\eta_O/\eta_{Si} \approx 2.0$—that is, stoichiometric growth. Excessive O(s) formation could occur when an already saturated Si(s) is exposed to the plasma in the form of direct silicon oxidation. Since this process is not likely at low deposition temperatures, the probability for direct Si oxidation was chosen to be small (1×10^{-4}). Having said that, ion sputtering during PE-ALD could expose Si(s) free radical sites that could be directly oxidized at low temperatures. For process conditions that are employed in HVM, the sputtering probability is low, which results in low direct oxidation. A major part of the oxidation is during precursor dosing to produce SiH_2(s), which is then oxidized to OH–Si–OH(s). Film growth does not significantly rely on the direct oxidation of Si(s) for these conditions.

The stoichiometry of the film is slightly Si rich throughout the deposition. This slight tendency toward Si richness results from SiH bonding that remains in the film due to the roughness of the film or codeposition that blocks sites from the incoming precursor or ROS. This SiH bonding is then grown over. However, the model does not include ROS diffusion through the film that might be capable of oxidizing SiH and producing a more stoichiometric film.

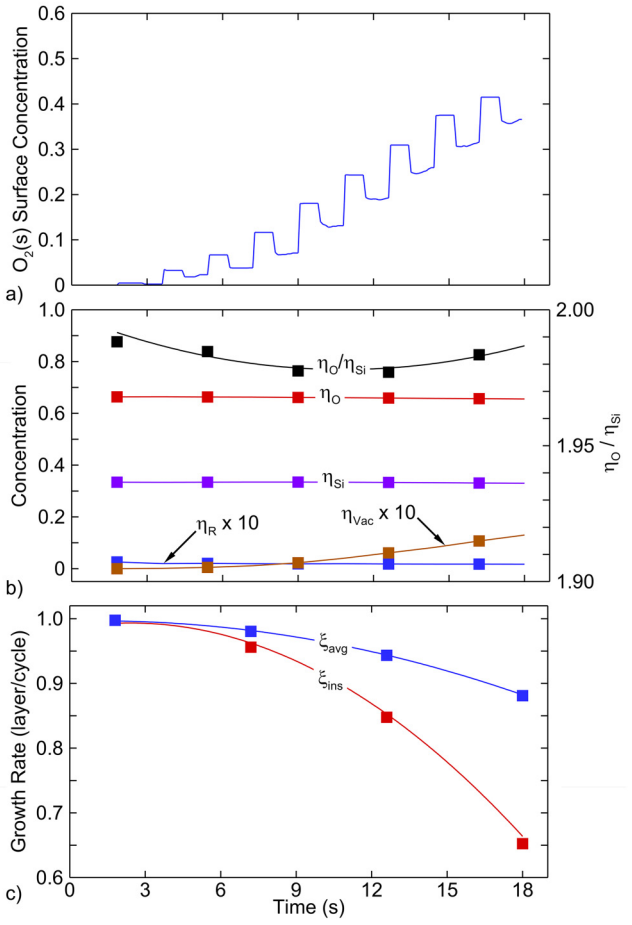

FIG. 6. SiO_2 blanket film properties as a function of time for the base case conditions (500 W, 10 MHz, 2 Torr, Ar/O_2 = 4/1 at 5 slm). (a) O_2(s) surface coverage. (b) Concentrations of oxygen, silicon, vacancies, and the ligand group, and the oxygen to silicon ratio in the entire film. (c) Time-averaged and instantaneous film growth rates.

The ligand group codeposition probability, $p_R = 0.005$, is constant throughout the ALD process, resulting in $\eta_R \approx 0.2\%$ being nearly constant while the film becomes rougher, more disordered, and more porous as it thickens. The vacancy density increases to 1% by the end of the tenth cycle. The rougher surface ultimately results in more bridging and, therefore, more vacancies. From a practical matter, we expect that during even nominal annealing, the trapped ligand groups are likely removed from the film, which then may add to the porosity, leading to a final postanneal porosity of about 1.2%.

The average (ξ_{avg}) and instantaneous (ξ_{ins}) film growth rates are shown in Fig. 6(c). A growth rate of one-layer/cycle would be

an ideal PE-ALD of SiO_2, represented here by two computational layers. ξ_{avg} is calculated by dividing the spatially averaged film thickness by the number of cycles, while ξ_{ins} is the increase in the film thickness relative to the prior cycle. (The film thickness is averaged in the center of the blanket deposition over a 10×10 nm^2 area.) Both ξ_{avg} and ξ_{ins} decrease with time for the first ten cycles, partly due to the roughness of the surface with "nooks and crannies" which provides steric hindrance to incoming reactants. ξ_{ins} decreases much from 1 (ideal to begin with) to a 0.6 layer/cycle in ten cycles. In practice, ξ_{ins} is often <1 layer/cycle.

Measurements of impurities in the PE-ALD of SiO_2 indicate relatively low values for optimized films. The PE-ALD of SiO_2 using O_2 plasmas at room temperature and 200 °C with BDEAS precursor produced less than 5% carbon impurity (detection limit) and 7%–10% hydrogen content.[35,36] PE-ALD-produced SiO_2 films, inspected using secondary ion mass spectroscopy, had 1%–3% carbon and nitrogen impurities.[37] Direct correlations between impurity level and surface roughness were not made. However, our results are consistent with low levels of impurity (<1%) corresponding to dense and smooth films, as observed experimentally, and higher levels of impurities corresponding to rougher and less dense films.

The PE-ALD of SiO_2 was also investigated in a trench, shown in Fig. 7. The process flow and reaction mechanisms are the same as the just discussed blanket deposition—the precursor dosing is 0.8 s and the plasma exposure is 1.0 s. The initial width (W) of the trench is 30 nm and the height (H) is 120 nm, producing an aspect ratio of 4. The depth (D) of the simulation domain is 10 nm with reflective boundary conditions. The voxels are cubes 0.5 nm on a side—70 (W) × 243 (H) × 20 (D) voxels. A trench is nominally a 2-dimensional structure and so could, in principle, be simulated in two dimensions. However, we have found that simulating nominally two-dimensional structures in three dimensions having a finite depth provides more realistic properties.

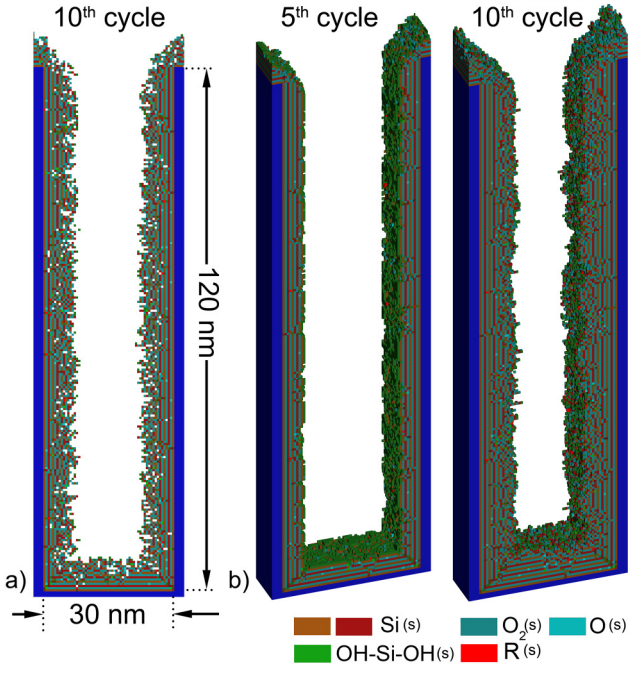

FIG. 7. PE-ALD grown SiO_2 films in a trench with AR = 4 for the base case conditions. (a) 2D film slice through the feature at the end of the tenth cycle. (b) 3D film profiles at the end of the fifth and tenth cycles. The initial trench dimensions are 30 nm (W) × 120 nm (H) × 10 nm (D) with reflective boundary conditions in depth.

The film deposited in a trench, similar to the blanket deposition, has a relatively uniform structure early in the process. These uniform and smooth surfaces become rougher, more disordered, and porous as the film grows thicker during the first ten cycles of the deposition. This effect is exacerbated by conduction limits, which do not apply to a blanket deposition (a flat surface). Conduction limits occur in the diffusion of gas atoms and molecules into high aspect ratio features. Particles diffusively reflecting from sidewalls have an equal probability of leaving the surface with a velocity component pointing upward toward the opening of the feature as pointing downward into the feature. Due to these conduction limits, neutral fluxes reaching surfaces deep in the feature are often smaller than those near the top. This decrease of flux is more pronounced if the particle has a surface reaction probability that can deplete the flux as it travels downward into the feature.[38] For example, the O atom flux during the plasma step of the first cycle at the top of the feature is 1.6×10^{18} cm^{-2} s^{-1}, whereas the flux at the bottom of the feature is 9.7×10^{17} cm^{-2} s^{-1}, a reduction of 40%. The oxidant fluxes are high enough that even at the bottom of the feature, the deposition is ordered with few defects during the first several cycles. However, as the feature fills, the aspect ratio increases, which worsens the conduction limits. This is particularly the case for O_2* flux, which is more reactive on the sidewalls than O atoms.

Fractional concentrations of the solid materials and vacancies, η_O/η_{Si}, and average and instantaneous growth rate at the bottom of the trench are shown in Fig. 8. The fractional concentrations are computed for the entire film. Similar to blanket deposition, when depositing a SiO_2 film in the trench, concentrations of Si and O are relatively stable in the first ten cycles, providing $\eta_O/\eta_{Si} \approx 1.9$, slightly Si rich. This is partly caused by a lack of oxidants deep in the trench due to conduction limits. This could be addressed by a longer plasma exposure step. At the end of the tenth cycle, η_O/η_{Si} is 1.95 in the top half of the trench and 1.88 in the bottom half, indicating a significant nonstoichiometric growth at the bottom.

As the film grows thicker, the aspect ratio of the feature increases from 4 to 4.8 after ten cycles, which further exacerbates the conduction limits. This narrowing of the feature significantly affects the O_2* flux. Due to the increasing conduction limits, by the end of the tenth cycle, the O_2* flux to the bottom of the feature has decreased by a factor of 4 compared with flux during the first cycle. At the same time, the O flux to the bottom of the feature remains almost the same. As surface sites are oxidized by O atoms, they become less reactive to the O atoms other than by physisorption and recombination.[38] So, as the O atoms are consumed by oxidation of the surface making those sites unreactive, the flux of O atoms is increased to lower sites in the feature.

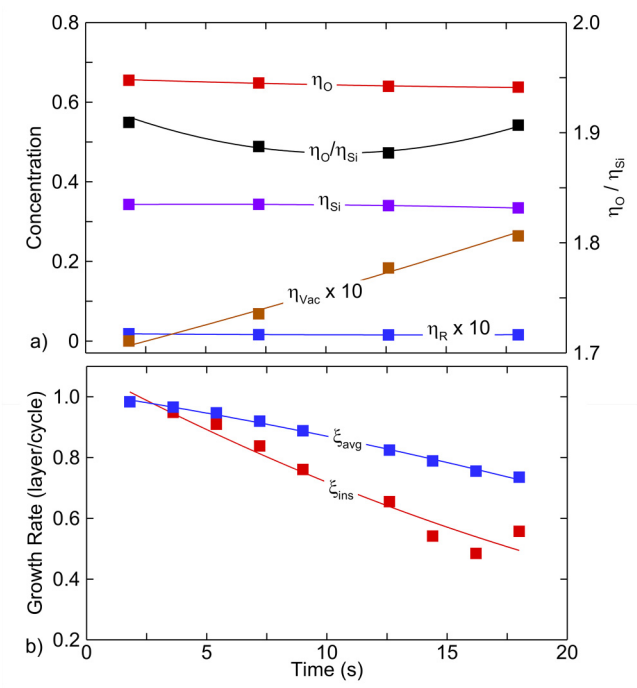

FIG. 8. SiO_2 film properties in a trench with AR = 4 as a function of time for the base case conditions. (a) Fractional concentrations of oxygen, silicon, vacancies, and the ligand group, and the oxygen to silicon ratio in the entire film. (b) Time-averaged and instantaneous film growth rates at the bottom of the feature.

In blanket deposition, the primary oxidants are O and O_2*. When depositing in a HAR feature, the main oxidant is O rather than a combination of O and O_2*, a disparity resulting from the quenching of O_2* that becomes more severe with depth into the feature and an increasing aspect ratio with a thickening film. Since the oxidation by O is a multistep process, insufficient oxidation would be more likely in a HAR feature than in blanket deposition in which O_2* is not quenched on the sidewalls. This reduction in ROS fluxes explains the lower η_O/η_{Si} in the bottom of the feature. With a decrease in oxidizing fluxes, the deposition rate drops from 1 to 0.5 layer/cycle in ten cycles.

After ten PE-ALD cycles, the predicted film roughness ranges from essentially smooth films for optimized conditions (i.e., negligible codeposition and fully saturated processing) to as large as 0.5–2.5 nm for conditions far from optimum (i.e., significant codeposition with poor saturation). Measurements of the RMS surface roughness for a well-optimized blanket PECVD of SiO_2 using a variety of precursors range from 0.08 to 0.5 nm.[39–42] Measurements of roughness on the sidewalls of HAR features have not been performed as a function of aspect ratio. Such measurements would be key validating data for the model.

A. Power

The EADs of Ar^+ and O with capacitively coupled powers of 400 W and 1 kW are shown in Fig. 9(a). Neither the ion energy and angular distribution (IEAD) nor the neutral energy and angular distribution (NEAD), incident onto the wafer, significantly changes as a function of power. For this reactor, power is applied through the blocking capacitor connected to the top electrode—the RF potential and DC bias are not applied to the substrate. As a result, the IEAD is affected only by the oscillation of the plasma potential with respect to ground. For a given RF voltage amplitude, the oscillation of the plasma potential with respect to ground decreases with a more negative DC bias. For 400 W, the RF amplitude and DC bias were 330 and −11 V. For 1000 W, the RF amplitude and DC bias are 495 and −130 V. The higher power produces a more asymmetric plasma that results in a more negative DC bias relative to the RF amplitude. As shown in Fig. 9(a), with the increase in power, the maximum Ar^+ energy is increased by only ≈5 eV from 40 to 45 eV, but the majority of the ions have lower energy, less than 5 eV, due to the highly collisional sheath.

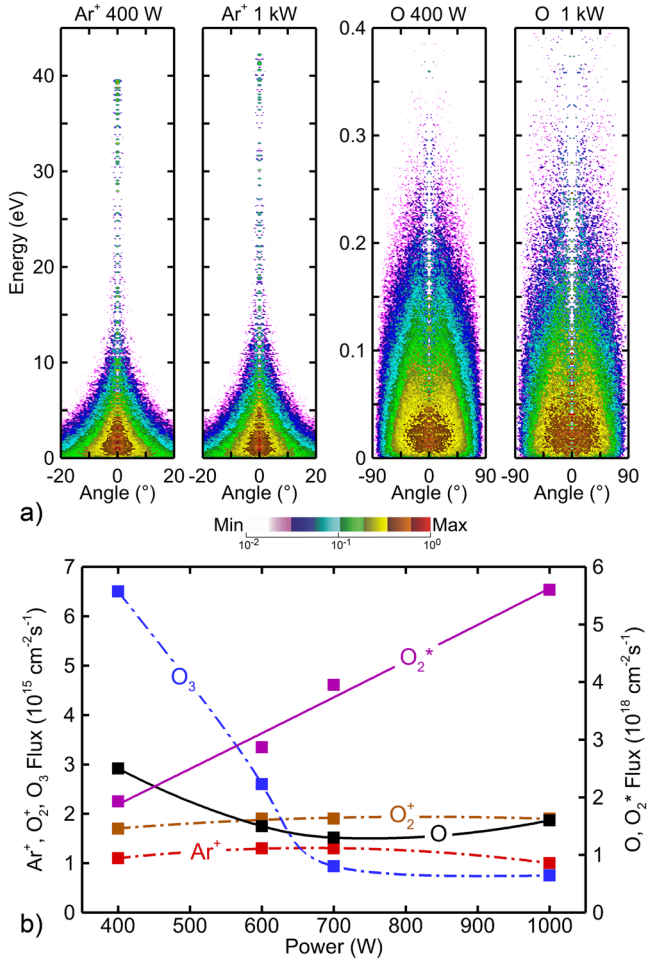

FIG. 9. Plasma properties as a function of power deposition for otherwise the base case conditions. (a) EADs of Ar^+ and O onto the wafer for powers of 400 W and 1 kW. (b) Fluxes of major reactants at the midradius of wafer.

In spite of the increase in power, the majority of that power is dissipated by ion accleration and electron heating in the vicinity of the sheath of the powered electrode. As a result, there are only nominal changes in the ion fluxes to the grounded substrate as a function of power, as shown in Fig. 9(b). The similar IEADs and ion fluxes suggest that there will be only small changes in sputtering as a function of power. The NEAD is also nearly constant when varying power over this range. The suprathermal tail of the NEAD results from charge exchange reactions, which also depend on ion fluxes, that are almost constant with varying power.

The fluxes of some ROS have notable variations with power that can potentially affect SiO_2 film deposition. As the power increases from 400 W to 1 kW, the O_3 flux decreases by a factor of nearly 10, from 6.5×10^{15} to 7.5×10^{14} cm^{-2} s^{-1}, owing to a decrease in the O_3 density caused by additional dissociative reactions and gas heating. At the same time, the excited state O_2* density increases with power from 1.9×10^{18} cm^{-2} s^{-1} at 400 W to 5.6×10^{18} cm^{-2} s^{-1} at 1 kW, which could provide the potential for an increased growth rate. However, with a plasma exposure time of 1 s, the deposition is already close to self-limiting at even powers of 400–500 W. Therefore, any increase of the film growth rate with power will not be large.

SiO_2 film components for blanket PE-ALD and growth rates are shown in Fig. 10 as a function of power at the end of the fifth cycle. As expected, with a long enough plasma exposure time to ensure that all conditions are in the saturated regime, changing the power has a limited effect on the film quality. Since the sputtering threshold is 30 eV, which is higher than the energy of most ions, damage due to ion bombardment is negligible. For these conditions, ordered growth of the oxygen and silicon layers occurs throughout the first five cycles, as shown at the top of Fig. 10. With an increase in the O_2* flux with increasing power, there is a small increase of the η_O/η_{Si} ratio toward the stoichiometric value of 2.0. Both the average and the instantaneous growth rates are close to 1 layer/cycle with varying power. The lower instantaneous growth rate is due to the onset of roughening as the film thickens. Using a silicon precursor BTBAS and a CO_2 plasma as the oxidant, Zhu *et al.* also found that the SiO_2 film growth rate is not particularly sensitive to plasma power provided that the power is high enough to produce saturating fluxes to the substrate.[43] A similar observation was made in the PE-ALD of Al_2O_3.[44] Over an intermediate range of powers, Lee *et al.* found that the SiO_2 growth rate was insensitive to power.[45] Using DIPAS and O_2 plasmas of sufficient power to provide saturating fluxes, the growth rate only marginally decreased at higher powers, an effect attributed to etching or damage by ion bombardment.

Even though input power has little effect on film deposition for these conditions because the plasma step is saturated, there will be more sensitivity for shorter plasma exposure times that may not result in fully saturated conditions. The consequences of plasma exposure time are discussed below.

The PE-ALD of SiO_2 was investigated in moderate aspect ratio trenches (AR = 4) as a function of power. Fractional concentrations of the solid materials and vacancies in the entire film, η_O/η_{Si}, and average and instantaneous growth rates at the bottom of the trench are shown in Fig. 11. Varying power has a more significant impact on deposition in the trench than blanket deposition. As the power

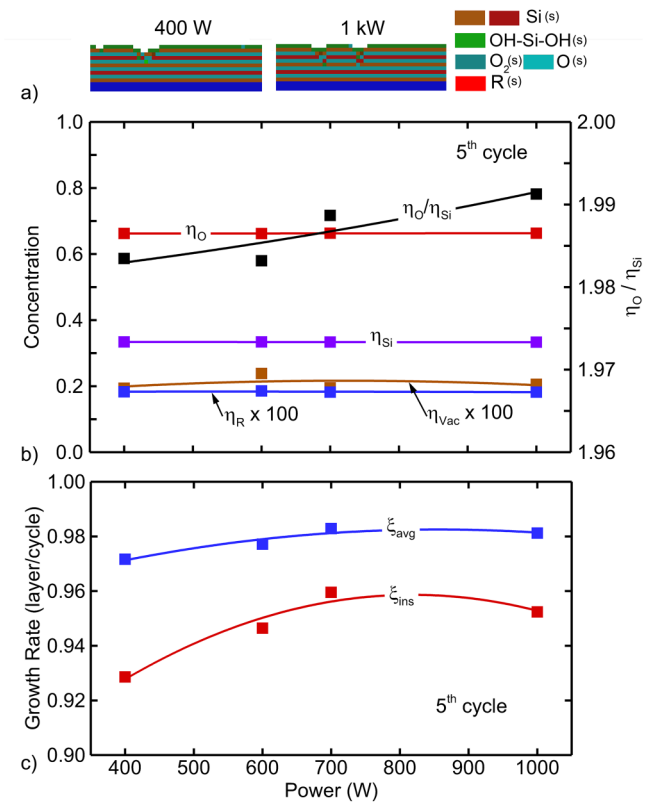

FIG. 10. SiO_2 blanket film properties as a function of plasma power at the end of the fifth cycle. (a) Cuts through the 3D surface for 400 W and 1 kW. (b) Fractional concentrations of oxygen, silicon, vacancies, and the ligand group, and the oxygen to silicon ratio in the entire film. (c) Time-averaged and instantaneous film growth rates.

increases from 400 to 700 W, the η_O/η_{Si} ratio decreases from 1.94 to 1.85 and then rises to 1.9 at 1 kW. This nonmonotonic of η_O/η_{Si} is mainly caused by the change of η_O owing to the variation in ROS fluxes with power. Film oxidation in a trench heavily relies on O instead of O_2* due to the quenching of O_2* on the sidewalls. Therefore, even though the flux of O_2* increases with power, it has little effect on film deposition deep in the trench. At 1 kW, at the end of the fifth cycle, the O_2* flux is 2.8×10^{17} cm^{-2} s^{-1} at the bottom of the trench compared with 6.9×10^{17} cm^{-2} s^{-1} for the O flux. As a result, film quality is more highly correlated with the the magnitude of O flux. Lower O fluxes lead to less oxidation, which generally produces more defects.

B. Pressure

The IEAD incident onto the substrate is sensitive to the collisions of ions transiting the sheath and so is sensitive to gas pressure. Increasing pressure makes a sheath more collisional, which broadens the ion angular distribution and reduces the overall ion energy onto the substrate. At the same time, with decreasing

pressure, ions transit the sheath with fewer (or no) collisions, resulting in higher ion energies up to the maximum of the sheath potential. Reactant fluxes to the wafer are also sensitive to pressure. To investigate the consequences of these trends on the PE-ALD of SiO_2, the pressure during plasma exposure was varied from 0.5 to 2 Torr, while keeping power constant at 500 W as in the base case.

The EADs of Ar^+ and O for pressures of 0.5 and 2 Torr are shown in Fig. 12(a). Ion energies striking the wafer are shown in Fig. 12(b). The maximum ion energy extends above 50 eV at 0.5 Torr and above 40 eV at 2 Torr. Even though the extent of the IEAD differs by only 10–15 eV, the IEAD at 0.5 Torr is more highly populated above 30 eV, the sputtering threshold. The higher ion energy at low pressure is collectively produced by a higher plasma potential and lower collision frequency. At 0.5 Torr, the plasma potential is 170 V, which decreases to 138 V at 2 Torr. As pressure increases from 0.5 to 2 Torr, the mean free path of Ar^+ shortens from 0.1 to 0.02 mm, resulting in more collisions as ions are accelerated through the sheath, dissipating ion energy. The EADs of neutral species are not significantly affected by pressure over the range of 0.5–2.0 Torr.

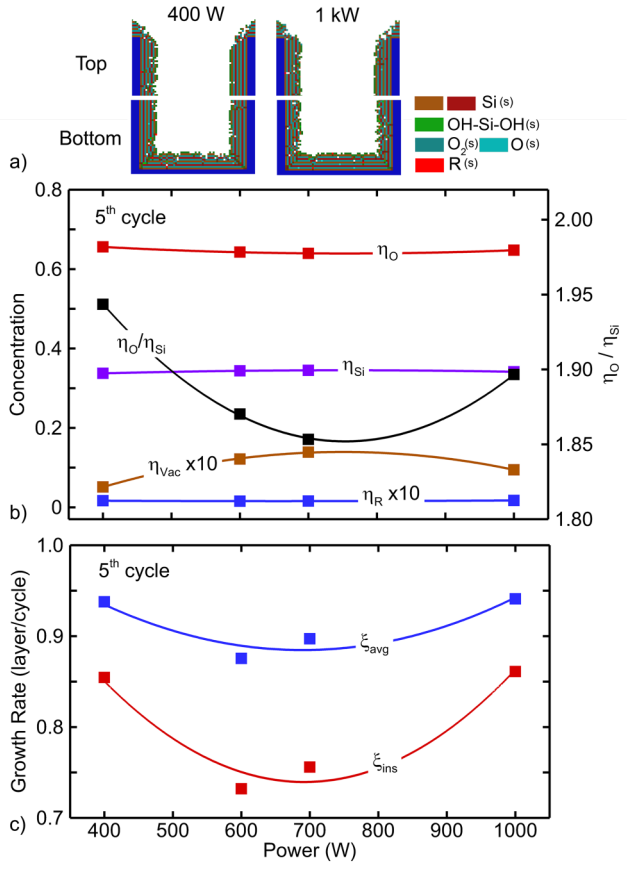

FIG. 11. SiO_2 film properties in a trench as a function of plasma power at the end of the fifth cycle. (a) Cuts through the 3D surface for 400 W and 1 kW at the top and bottom of the trench. (b) Fractional concentrations of oxygen, silicon, vacancies, and the ligand group, and the oxygen to silicon ratio in the entire film. (c) Time-averaged and instantaneous film growth rates at the bottom of the trench.

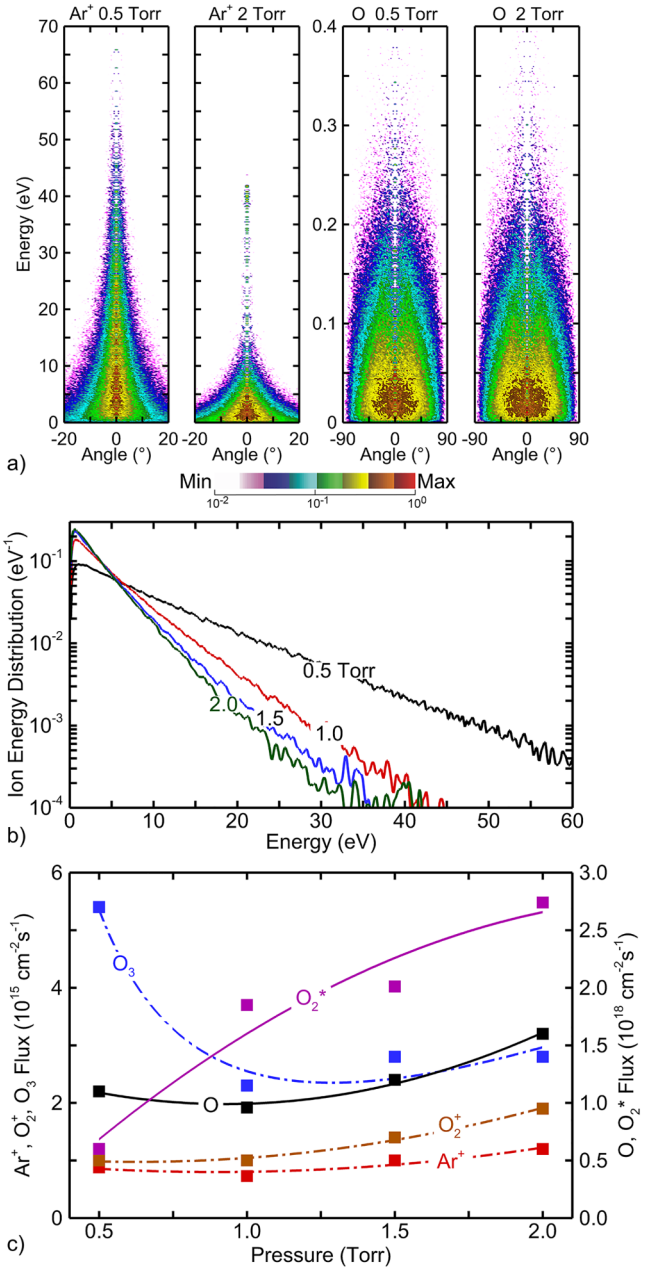

FIG. 12. Plasma properties as a function of pressure for otherwise the base case conditions (a) EADs of Ar^+ and O onto the wafer for pressures of 0.5 and 2 Torr. (b) Energy distributions function of all positive ions onto the wafer for pressures of 0.5–2.0 Torr. (c) Fluxes of major species at the midradius of the wafer.

The fluxes to the substrate of major reactive species (O, O_2*, O_3, O_2^+, and Ar^+) are shown in Fig. 12(c). Generally, increasing pressure produces an increase in fluxes as higher pressure leads to higher rates of ionization and excitation and less power dissipated in ion acceleration in the sheath that does not produce gas-phase excitation. The higher ion fluxes at higher pressures are, however, delivered to the substrate with lower energy. Therefore, their effect on the SiO_2 deposition process is small. The O_3 flux decreases with an increasing pressure due to increased rates of electron collision quenching. On the other hand, increased pressure leads to an increase of the fluxes of two major oxidants, O and O_2*. The combined fluxes of O and O_2* increased by a factor of 3 from 0.5 to 2.0 Torr.

Film composition and growth rates as a function of pressure for blanket deposition of SiO_2 are shown in Fig. 13. The film properties have only minor changes for pressures exceeding 1 Torr. At lower pressures, the increase in the energy of the incident ions produces sputtering that damages the film, largely by producing vacancies and removing oxygen. The removal of oxygen lowers the η_O/η_{Si} ratio to 1.85 at 0.5 Torr from being nearly stoichiometric at 2.0 Torr. The vacancy fraction of 1.5% at 0.5 Torr produces rough and disordered films. The nonideality of the films at low pressure is in part due to the lower fluxes of O and O_2*, resulting in nonoxidized SiH_2(s) surface sites that lead to vacancies.

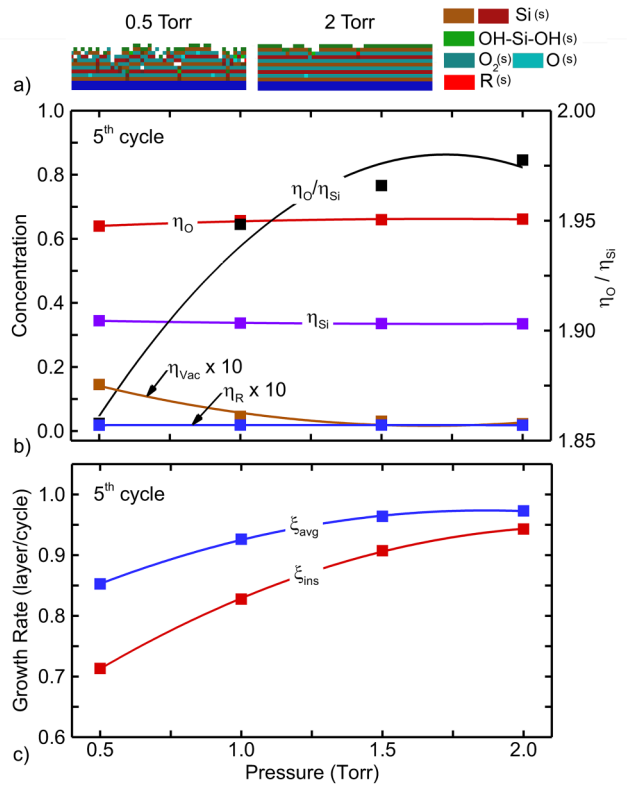

FIG. 13. SiO_2 blanket film properties as a function of pressure at the end of the fifth cycle. (a) Cuts through the 3D surface for 0.5 and 2 Torr. (b) Fractional concentrations of oxygen, silicon, vacancies, and the ligand group, and the oxygen to silicon ratio in the entire film. (c) Time-averaged and instantaneous film growth rates.

The film growth rates monotonically decrease with decreasing pressure, a trend caused in large part by the lack of ROS and by ion bombardment sputtering. A lack of ROS results in nonsaturated oxidation and a residue of SiH_2(s) sites at the end of plasma exposure. Such SiH_2(s) sites are unreactive with the silicon precursor SiH_2R_2. Therefore, the residual SiH_2(s) sites can be oxidized only during the following plasma exposure step. In this case, a layer of SiO_2 is deposited in two cycles instead of one cycle, resulting in a lower deposition rate. Sputtering produces disorder in the layers, which generally lowers the deposition rate. For example, if a SiH_2(s) site is sputtered from the surface at the beginning of a plasma exposure step, the exposed O_2(s) site must wait at least to the following precursor exposure step to be passivated with SiH_2(s). Again, it takes two cycles instead of one cycle to deposit a monolayer of SiO_2 at that position, compared with a nonsputtered neighboring site. The spatially averaged layer thickness is then smaller and the surface rougher.

The results of the simulations of film deposition for varying pressure in a trench are presented in Fig. 14. Increasing the pressure results in higher ROS fluxes to the bottom of the trench. The relatively broad ion angular distribution results in less ion bombardment deep in the trench with lower energy and so less damage. These trends result in a higher η_O/η_{Si} ratio, lower vacancy fractional concentrations, and higher film growth rates at higher pressures. At the end of the fifth cycle, the vacancy concentration decreases by a factor of 2 from 2.1% to 1.1% when increasing the pressure from 0.5 to 2 Torr. However, for blanket deposition, vacancies decrease by a factor of 7, from 1.5% to 0.2%, over the same range of pressure. The vacancy concentration decreases less with pressure for PE-ALD in a trench because conduction limits constrain the ROS fluxes to the bottom of the trench. Ion bombardment damage to the film is also not as significant in a trench as for blanket deposition. A part of this lack of sensitivity to ion bombardment in the trench is that even for these broad angular ion distributions, ions striking the sidewalls of the trench do so with grazing angles for which sputtering yields are low. Arts *et al.* found that the oxygen surface recombination probability corresponding to reaction (10a) decreases from 10^{-4} to 10^{-5} as pressure increases from 10 to 130 mTorr.[46] This recombination reduces O atom flux into features having a large aspect ratio. As a result of the decrease in recombination probability, for a given plasma exposure time, film growth penetrates deeper into a HAR trench with higher quality with increasing pressure.

C. Codeposition probability

Steric hindrance occurs when ligands from the precursor fail to react with hydrogen atoms on the surface and remain bonded to the silicon or are adsorbed on the surface. Ligands may block nearby sites from reacting with the gas-phase particles and hinder the deposition process. In the current mechanism, steric hindrance is addressed by codepositing a ligand group R(s) along with the precursor with probability p_R with the default value being 0.005.

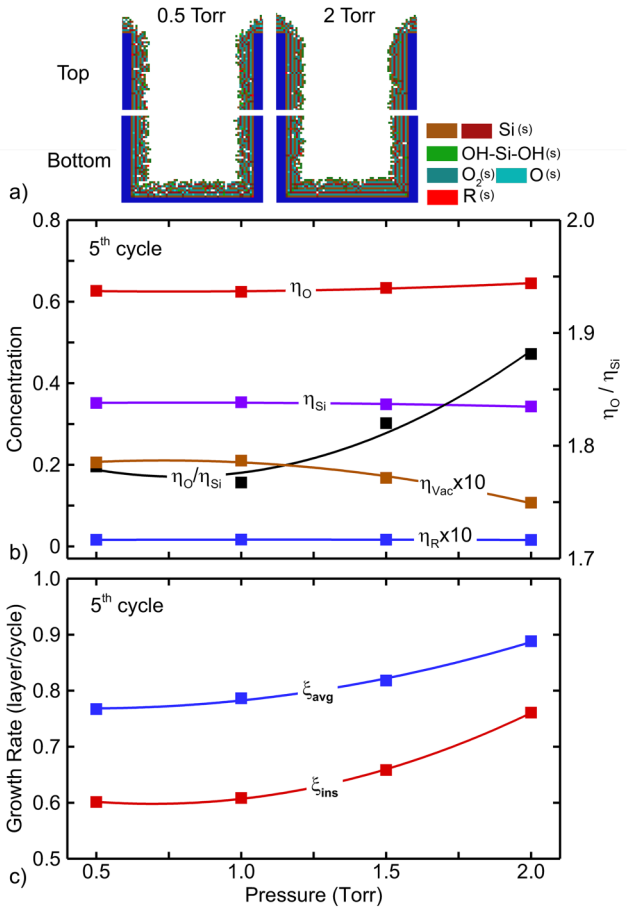

FIG. 14. SiO_2 film properties in a trench as a function of pressure at the end of the fifth cycle. (a) Cuts through the 3D surface for 0.5 and 2 Torr at the top and bottom of the trench. (b) Fractional concentrations of oxygen, silicon, vacancies, and the ligand group, and the oxygen to silicon ratio in the entire film. (c) Time-averaged and instantaneous film growth rates at the bottom of the trench.

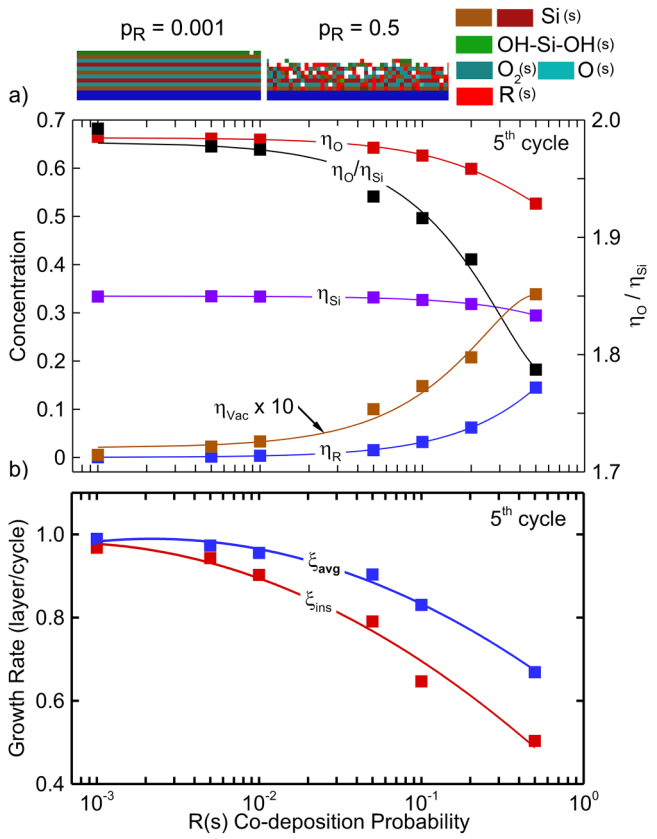

FIG. 15. SiO_2 blanket film properties as a function of the codeposition probability p_R for the ligand group at the end of the fifth cycle. (a) Cuts through the 3D surface for $p_R = 0.001$ and 0.5. (b) Fractional concentrations of oxygen, silicon, vacancies, and the ligand group, and the oxygen to silicon ratio in the entire film. (c) Time-averaged and instantaneous film growth rates.

In this section, we discuss the consequences of p_R on SiO_2 film quality.

Film properties and growth rates as a function of p_R (0.001–0.5) for blanket deposition are shown in Fig. 15. The effect of p_R becomes consequential when $p_R \geq 0.01$. As p_R increases, both oxygen and silicon concentrations decrease. The R(s) deposition directly affects η_{Si} since codeposition occurs during precursor dosing. A codeposited R(s) blocks an oxygen site that might otherwise receive the precursor to form SiH_2(s). Therefore, with a high p_R, it is unlikely to fully saturate the surface with SiH_2(s) at the end of precursor dosing, which then leads to a lower η_{Si}. However, it is also possible for R(s) to be codeposited on top of the deposited SiH_2(s) and occupy voxels in the next oxygen layer. With the same SiH_2R_2 flux and the same deposition probability of SiH_2(s), a higher p_R results in more R(s), thus less OH–Si–OH(s) following the plasma exposure step.

When $p_R > 0.01$, η_O decreases more rapidly than η_{Si}, leading to a decrease in η_O/η_{Si} from 1.97 at $p_R = 0.01$ to 1.79 at $p_R = 0.5$. The increase in R(s) concentration (η_R) produces roughness in the film, which allows for bridging reactions and the formation of vacancies. As p_R increases from 0.05 to 0.5, vacancies increase from 1% to 3%. Note that in many applications, after deposition, the ligand remnants are removed through annealing such that the final vacancy concentration in the film is $\eta_{Vac} + \eta_R$. (This assumes that there is no densification of the film during annealing.) In that scenario, the vacancy concentration reaches 2.5% when $p_R = 0.05$. As described earlier, the growth rate of a film decreases as the surface becomes rougher. Decreases in both average and instantaneous growth rates occur when p_R increases from 0.001. When $p_R = 0.001$, the deposition process is almost ideal with a growth rate of 1 monolayer per cycle. At $p_R = 0.5$, the instantaneous growth rate decreases to 0.4 layer/cycle at the fifth cycle.

The results for film deposition in a trench with a varying p_R are given in Fig. 16. The results are similar to those for blanket deposition. At the end of the fifth cycle, with an increase in p_R

from 0.001 to 0.5, η_O/η_{Si} decreases from 1.89 to 1.69, η_{Vac} increases from 1% to 3%, and η_R increases from 0.03% to 15%. When p_R is small, insufficient oxidation caused by a low oxidant fluxes already produces a η_{Vac} of 1%. This high vacancy concentration overshadows the impact of increasing p_R until $p_R \geq 0.05$. These same trends occur for the instantaneous film growth rate. Owing to conduction limits, the instantaneous film growth rate at the fifth cycle is only 0.8 layer/cycle at the bottom of the trench even with a small p_R. A decrease in ξ_{ins} occurs when $p_R \geq 0.01$. Before that point, the impact of p_R on the growth rate is outweighed by the effects of conduction limits of ROS on the growth rates.

The value of p_R affects precursor dosing. Dosing is an isotropic thermal process that is not significantly affected by the topology of the target feature provided that the precursor step is long enough to reach saturation. Therefore, η_R is qualitatively similar for blanket deposition and deposition in a trench as a function of p_R. However, due to the conduction limits, the ligand remnants in the bottom of a trench are less likely to be removed by sputtering and oxygen insertion reactions. The vacancies deep in the trench are less likely to be repaired by the later deposition steps. Therefore, with the same p_R, steric hindrance has a more severe impact for deposition in a trench than for blanket deposition.

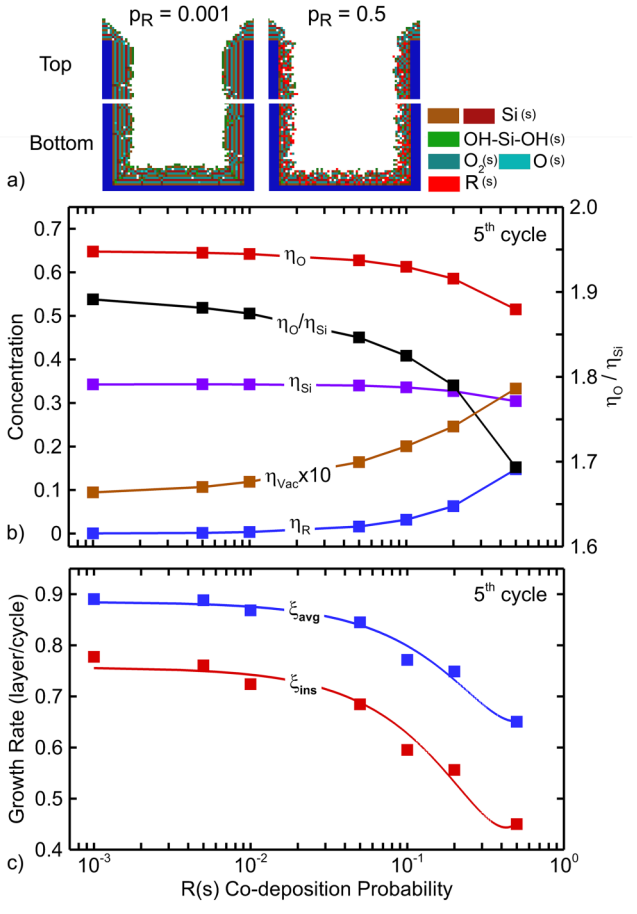

FIG. 16. SiO_2 film properties in a trench as a function of the codeposition probability p_R for the ligand group at the end of the fifth cycle. (a) Cuts through the 3D surface for $p_R = 0.001$ and 0.5 at the top and bottom of the trench. (b) Fractional concentrations of oxygen, silicon, vacancies, and the ligand group, and the oxygen to silicon ratio in the entire film. (c) Time-averaged and instantaneous film growth rates at the bottom of the trench.

D. Plasma exposure time

The imperfections in a SiO_2 film deposited using PE-ALD often result from insufficient oxidation. One remedy is to simply lengthen the plasma exposure time to ensure that the oxidation of the precursor produced sites, ideally consisting of SiH_2(s), has saturated. The saturated surface has all SiH_2(s) converted to OH–Si–OH(s). Nonsaturated, nonoxidized sites are unreactive to the next dose of precursor. In this section, the results from the simulation for plasma exposure times (τ_p) of 0.2–2 s with a precursor dosing of 0.8 s are discussed.

Film components and growth rates for a blanket deposition as a function of τ_p from 0.2 to 2 s are shown in Fig. 17 after the fifth

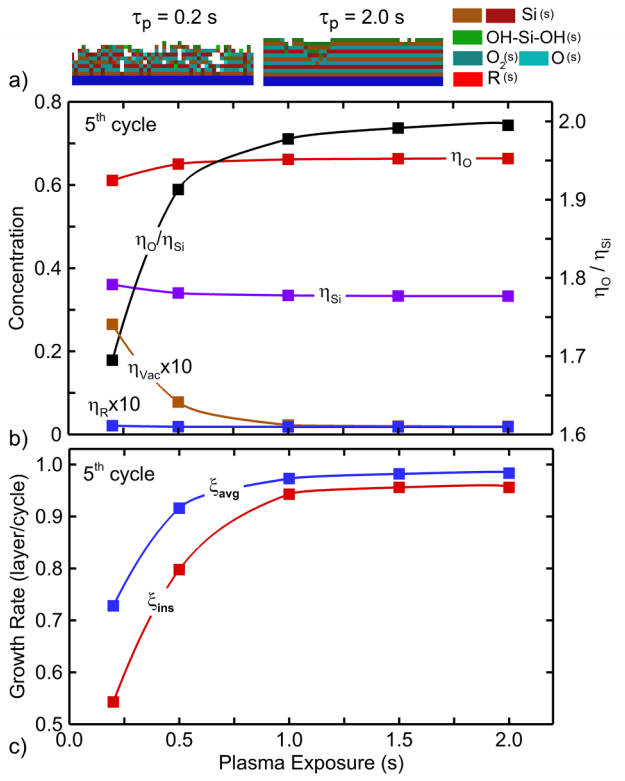

FIG. 17. SiO_2 blanket film properties as a function of the plasma exposure time τ_p at the end of the fifth cycle. (a) Cuts through the 3D surface for $\tau_p = 0.2$ s and 2.0 s. (b) Fractional concentrations of oxygen, silicon, vacancies, and the ligand group, and the oxygen to silicon ratio in the entire film. (c) Time-averaged and instantaneous film growth rates.

cycle. A long τ_p provides a large-enough ROS fluence to oxidize and saturate SiH_2(s) sites, providing a denser and more uniform surface for subsequent cycles. As τ_p increases from 0.2 to 2 s, η_{Vac} decreases by a factor of 12 from 2.4% to 0.2%, having reached the minimum level of vacancies for $\tau_p > 1$ s. Increasing τ_p also improves the stoichiometry, increasing η_O/η_{Si} from 1.7 at $\tau_p = 0.2$ to approaching 2 for $\tau_p = 2$ s. Similar porosity fractions and trends were measured by Lee *et al.*[45] for the PE-ALD of SiO_2 using DIPAS and O_2 plasmas. They found porosities of up to 5% at low plasma exposure time, decreasing to 2% at high exposure time, though this decrease was not monotonic. Zhu *et al.* measured an increase in film density with increasing plasma exposure time, which implies a decrease in porosity.[44] Measurements by Dingemans *et al.*[36] showed an increase in the index of refraction with increasing plasma exposure time, a result that implies higher density and lower porosity. Shin *et al.* measured a decrease in the wet-etch rate with increasing plasma exposure time that would imply a more dense film and lower porosity.[12]

Similarly, a significant increase of ξ_{ins} and ξ_{avg} occurs when increasing τ_p from 0.2 s ($\xi_{ins} = 0.54$, $\xi_{avg} = 0.72$) to 2 s ($\xi_{ins} = 0.96$, $\xi_{avg} = 0.98$). The convergence of the instantaneous and average growth rates indicates that the growth is self-limited with saturated oxidation. When τ_p is short (<1 s), the surface coverage of OH–Si–OH(s) is less than unity after plasma exposure due to the low oxidant fluence. As a result, silicon deposition during the following precursor dosing step is compromised, producing a growth of less than a monolayer per cycle. As τ_p increases, the surface approaches being saturated with OH–Si–OH(s) at the end of plasma exposure. These conditions are ideal for the succeeding precursor dosing. However, even at a long τ_p, the ligand remnants and the scarcely distributed nonoxidized sites after plasma exposure produce a smaller ξ_{ins} than ξ_{avg} but the difference between them is nominal (0.96 vs 0.98 layer/cycle). This saturation in the rate of film growth as a function of plasma exposure time was also observed by Lee *et al.*[45] A growth rate of 0.15 nm/cycle was achieved with a 0.5 s of O_2 plasma exposure time and 1 s DIPAS exposure. The growth rate was then constant up to 2 s of plasma exposure. Similar saturation with plasma exposure time was observed by Dingemans *et al.*[36] and by Jeon *et al.*[15]

Deposition of SiO_2 film in a trench while varying τ_p from 0.2 to 2 s was also investigated. The film composition and growth rates recorded at the bottom of the trench at the fifth cycle are shown in Fig. 18. Similar to blanket deposition, the stoichiometry and film growth rates increase with increasing τ_p. However, longer plasma exposure times are required to saturate the surface due to the conduction limits of ROS transporting into the feature. The porosity, growth rates, and stoichiometry at the bottom of the trench do eventually equal those of blanket deposition. To achieve this parity requires twice the plasma exposure time to overcome the conduction limits of ROS into the feature.

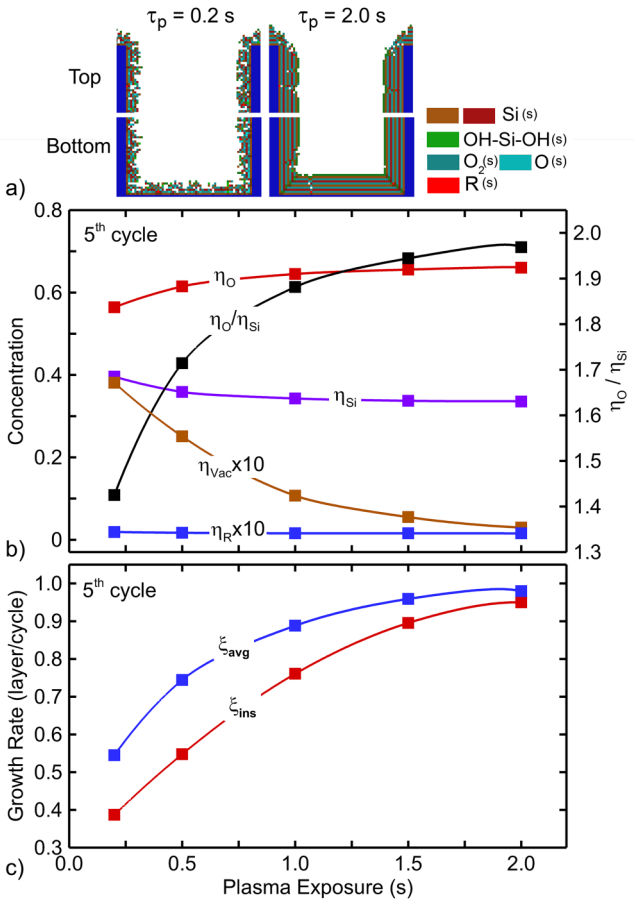

FIG. 18. SiO_2 film properties in a trench as a function of the plasma exposure time τ_P at the end of the fifth cycle. (a) Cuts through the 3D surface for $\tau_P = 0.2$ s and 2.0 s at the top and bottom of the trench. (b) Fractional concentrations of oxygen, silicon, vacancies, and the ligand group, and the oxygen to silicon ratio in the entire film. (c) Time-averaged and instantaneous film growth rates at the bottom of the trench.

E. Vias and aspect ratio

Conduction limits predominantly affect film deposition in high aspect ratio features and features that have large surface-to-volume ratios (SVRs). Reactants diffusing into features with large SVRs will have more collisions with the walls to reach a given depth. Vias (cylindrical holes) have larger SVR than trenches and so will be more sensitive to conduction limits resulting from deposition into high aspect ratio (AR) features.

To investigate the consequences of the aspect ratio, the PE-ALD of a SiO_2 film was simulated for deposition in vias. The diameter of the via was 30 nm, and the height was varied between 60 and 240 nm, providing an AR between 2 and 8. To reduce the computational burden of simulating an inherently three-dimensional structure, a 90° sector of the via was modeled with reflective boundary conditions being applied to all vertical boundaries, as shown in Fig. 19(a). The process flow consisted of a 0.8 s precursor dosing and 1 s plasma exposure.

Film deposition in an AR = 4 feature after PE-ALD cycles 2, 5, and 8 is shown in Fig. 19(a). Similar to deposition in a trench or blanket deposition, the SiO_2 layers deposited in the first several cycles are more uniform, having only sparsely distributed

imperfections and misalignments. There are artificial misalignments due to a cubic mesh being used to represent a circular structure, which produces unavoidable stair-stepping in the mesh. These artificial misalignments appear not to propagate into subsequent layers. However, defects such as vacancies, unoxidized SiH_2(s), and ligand remnants do act as seeds that propagate upward from the bottom of the via or laterally from the sides of the via. The gradual roughening, vacancies, and disorder are evident from the interior views of the vias. The time of the images corresponds to the postoxidation step at which time the surface of the perfect PE-ALD should be saturated with OH–Si–OH(s) groups. This is the situation for the cycle 2 feature. However, by cycles 5 and 8, the surface is nearly a random distribution of all of the surface species.

Vertical and horizontal cuts through vias for AR = 2, 4, 6, and 8 are shown in Fig. 19(b) at the end of the eighth cycle. The vertical cuts show the bottom 30 nm of the feature. The horizontal cut is taken about 20 nm from the bottom of the feature. The conduction limits of oxidizing fluxes to the bottom of the feature reduce their values as the AR increases. The sum of the fluxes of all oxidizing species to the bottom of the feature at the end of the third cycle decreases by a factor of 2.3 from AR = 2 to 8. The rate of decrease is larger in a via that is actively being processed than in a passive via due to the consumption of flux by reactions on the sidewalls. The reduction in oxidizing species with increasing AR leads to disorder and vacancies, which also increase with the number of layers. The nominally ideal PE-ALD structure is retained for the first 4–5 layers for AR = 2. This nominally ideal structure is retained for only the first two layers for AR = 8.

The fractional concentrations of vacancies and the elementary ratio η_O/η_{Si} at the end of the eighth cycle for vias and trenches as a function of AR are shown in Fig. 20(a). These values are for the bottom half of the trench or via. Growth rates as a function of AR for trenches and vias are shown in Fig. 20(b). The general trends for both vias and trenches at any AR are a lower η_O/η_{Si}, higher η_{Vac}, and lower growth rate than blanket films. Compared with trenches, vias have a lower η_O/η_{Si}, higher η_{Vac}, and lower growth rate. All of these trends can be attributed to the decrease in oxidizing fluxes due to the reactions on the sidewalls and conduction limits, both of which

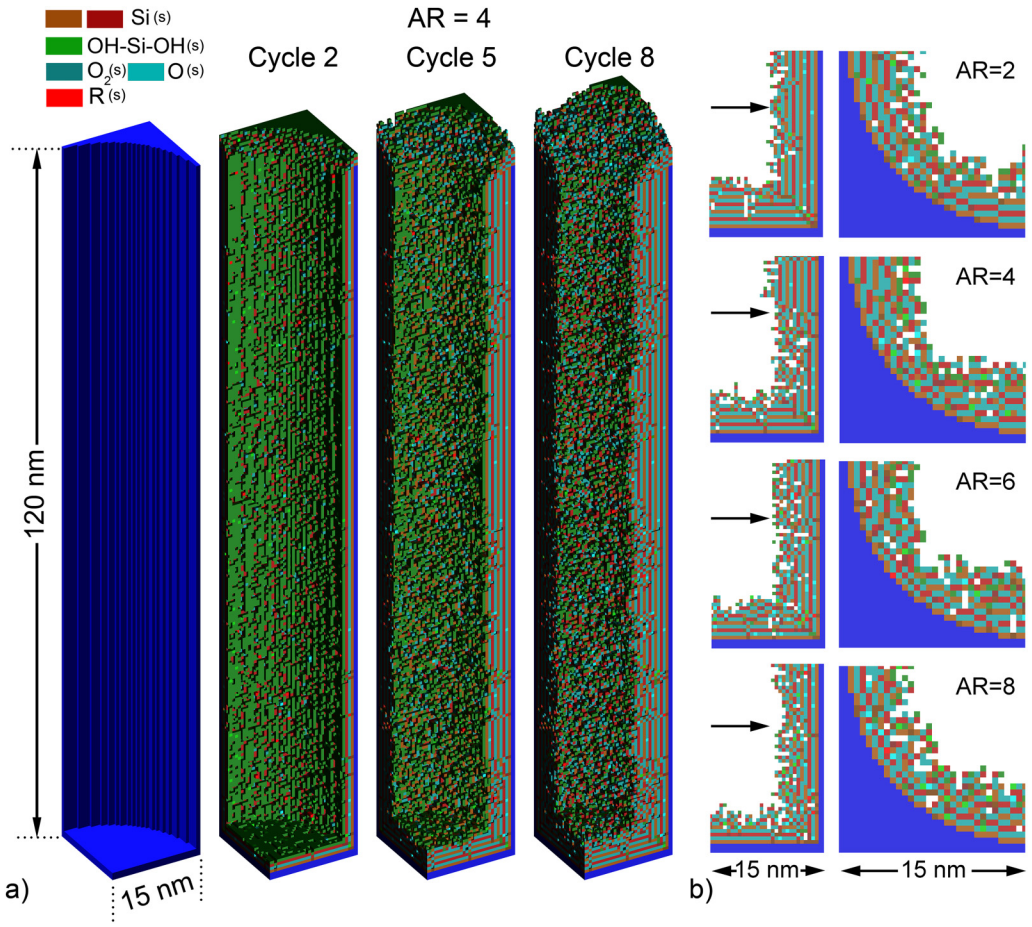

FIG. 19. Film properties for SiO_2 deposition in a via for the base case conditions. (a) Initial surface having an aspect ratio AR = 4 and a growing film after cycles 2, 5, and 8. (b) Axial and horizontal cuts through the via for AR = 2, 4, 6, and 8. The axial cut is at the bottom of the feature. The horizontal cut is at the height shown by the arrow.

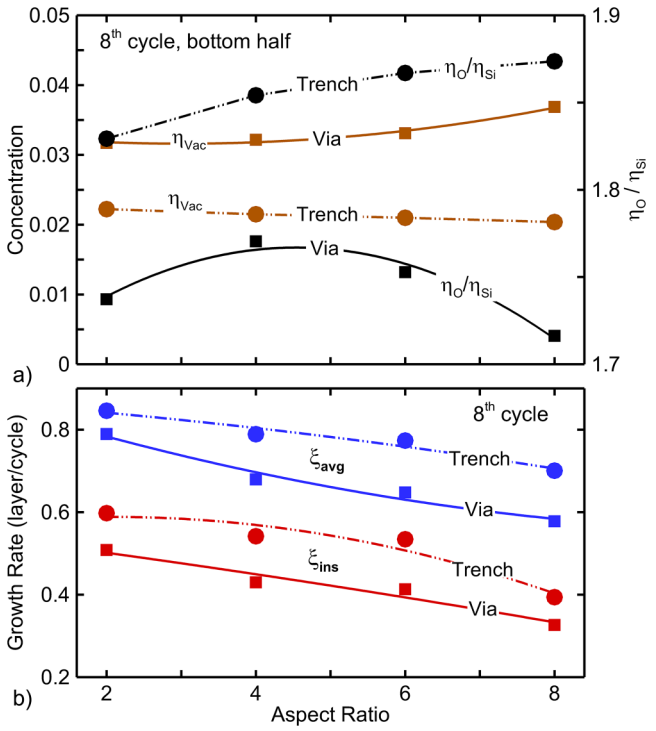

FIG. 20. Film properties as a function of AR for deposition in a via and trench after the eighth cycle. (a) Fractional concentrations of vacancies and O/Si ratio for the bottom half of the feature. (b) Time-averaged and instantaneous film growth rates at the bottom of the feature.

are more severe with a larger SVR—a via has a higher SVR than a trench when its AR is the same. The ratio of SVR for a via compared with a trench is 1.5 for AR = 2 and 1.9 for AR = 8. This increase in the surface-to-volume ratio produces more severe conduction limits that restrain the fluxes to the bottom of the feature and provides more relative surface area for reactions to consume (or quench) reactive species while transporting to the bottom of the feature. For example, for our base case plasma conditions during the first plasma exposure, with AR = 8, the O flux to the bottom of a trench is 9.0×10^{17} cm^{-2} s^{-1}, as compared with 2.0×10^{17} cm^{-2} s^{-1} in the via. The decrease of flux in the via is even more significant for more reactive species such as O_2*, whose flux is 1.1×10^{17} cm^{-2} s^{-1} to the bottom of a trench while being 2.0×10^{15} cm^{-2} s^{-1} to the bottom of a via. These lower fluxes for vias result in a lower η_O/η_{Si}, higher η_{Vac}, and lower growth rate. These predictions are consistent with the measurements of Arts *et al.*[46], who found that increased plasma exposure times are required to saturate and maintain GPC as the aspect ratio increases. Similar observations were made by Putkonen *et al.*[26], who found that longer O_2 plasma exposure times were required to saturate growth rates in high AR features.

The scaling of the film growth rate with aspect ratio for vias and trenches follows expectations—lower growth rates as the AR increases due to the lower fluxes to the bottom of the feature. The scaling of η_O/η_{Si} and vacancies deep in the features with AR is less clear. The complicating factor is the contribution of ions. The solid angle for receiving ions into the feature is larger for a given aspect ratio for trenches compared with that for vias. For the broad angular distribution of ions incident onto the wafer, ions are, therefore, more influential in vias having a small aspect ratio than in those with a large aspect ratio. This larger relative contribution of ions at a low AR disproportionately reduces η_O/η_{Si} and increases η_{Vac}.

V. CONCLUDING REMARKS

PE-ALD of a SiO_2 film for the first ten cycles was computationally investigated at the reactor and feature scales. The reactor scale simulations were performed for an $Ar/O_2 = 80/20$ CCP. Fluxes of reactants onto the wafer and their EADs predicted by the reactor scale model were used as an input to a voxel-based, three-dimensional feature scale model. In the base case, 500 W was applied to the top electrode of the CCP reactor to sustain an Ar/O_2 plasma at 2 Torr. The dominant reactive neutrals were $O_2(a^1\Delta_g)$, O, and $O_2(b^1\Sigma_g^+)$, all with close to thermal EADs onto the wafer. The dominant ions, Ar^+ and O_2^+, had an incident angle onto the wafer of less than 20° and energy less than 20 eV, which is lower than sputtering thresholds. These, as well as low ion fluxes, suggest an insignificant impact of ion bombardment damage to the film.

A deposition mechanism of SiO_2 using silicon precursors with two ligand groups and oxidation by the Ar/O_2 plasma was developed. The base case PE-ALD process consisted of repeated precursor dosing (0.8 s) and plasma exposure (1.0 s). Steric hindrance was addressed by codepositing a ligand site along with the silicon during precursor dosing with a specified codeposition probability p_R. The impact of the ligand remnants left in the film at an early stage of deposition, such as vacancies and disorder, was shown to increase as the film grows thicker over the first ten cycles. Since the silicon precursor cannot directly be deposited on the oxygen sites O_2(s), and because of the low sputtering rate, the surface coverage ratio of O_2(s) increases with time and produces a decrease in the instantaneous film growth rate. Film deposition in a trench follows many of the same trends as a blanket deposition. Vacancy concentrations increase, while the film growth rate decreases with increasing film thickness. Due to conduction limits, the film growth rate at the bottom of a trench decreases faster than that for blanket deposition.

The impact of power, pressure, codeposition probability of the ligand remnant p_R, and plasma exposure time on blanket deposition and deposition in a trench was investigated. With a plasma exposure time of 1 s, the film growth was found to be nearly saturated and self-limiting. Therefore, neither concentrations of film components nor growth rates were overly sensitive to variations in input power for blanket deposition. However, conduction limits of the flux of oxidizing species through high aspect ratio features made the growth rate and η_O/η_{Si} sensitive to the change of ROS fluxes.

Varying the pressure was found to significantly affect film quality. Decreasing pressure produced lower ROS fluxes and a less collisional sheath, which enabled higher energy ions to reach the substrate. Using lower pressure during plasma exposure then resulted in vacancies and slower film growth. Varying the codeposition probability, p_R, of the ligand group had similar effects for both blanket deposition and deposition in a trench. At low $p_R < 0.05$, the film was

uniform and dense, while high $p_R \geq 0.05$ produced disordered and rough films with vacancies. Plasma exposure time (τ_p) was found to be an essential process parameter for controlling film quality. A longer τ_p ensured saturated oxidation, which is critical for depositing dense and stoichiometric films.

In principle. many of these AR-dependent processes and conduction limits can be remedied by increasing the fluence into the feature of plasma-produced ROS by, for example, lengthening the plasma exposure step. Increasing the fluence increases the likelihood of fully saturating the surface to produce OH–Si–OH(s) functionality after the oxidation step. This strategy would be the equivalent of an overetch period in the plasma etching of high AR features. However, as the fluence of ROS increases, the fluence of energetic ions also increases, which increases the likelihood for sputtering damage. Increasing the ROS fluence will also increase the rate of oxidizing and removing the ligand remnants in the film. Increasing the ROS fluences, while minimizing ion damage, implies operating at the highest practical pressures. A possible limitation of increasing the ROS fluence to address conduction limits is secondary reactions such as H abstraction by O atoms from OH–Si–OH(s) to produce O-radical sites.

Another possible limit of increasing the fluence of ROS is the consequence of also increasing the fluence of vacuum ultraviolet (VUV) radiation onto the surface. VUV photons can potentially affect the properties of the film. Although not included in the surface kinetics model, VUV radiation transport is included in the reactor scale model. For the $Ar/O_2 = 80/20$ gas mixture at 2 Torr, the VUV radiation onto the substrate is 1.5×10^{14} cm^2 s^{-1} and is dominated by the resonance lines of argon (105 nm, 107 nm). The absorption length of VUV radiation at these wavelengths by crystalline SiO_2 and quartz is a few nanometers with significant VUV fluences generally producing a higher trapped charge[47] and in some cases higher wet-etch rates.[48] Since exposure to VUV fluxes is cumulative, extending the plasma exposure step to ensure saturation will increase the VUV effects on thin films. For HAR features, this is unlikely to be a major concern since the incident VUV fluxes are isotropic. For low AR ratio features, this cumulative VUV exposure could be problematic.

This investigation was performed with the substrate temperature held constant at 50 °C where oxidizing processes are dominated by plasma-produced species. However, surface reaction probabilities are temperature dependent. In particular, in recent studies, Beladiya *et al.* found that local thermal spiking by ion bombardment during PE-ALD increases the probability for precursor attachment to oxygen sites, which leads to denser films.[49] This outcome has also been reported by Arts *et al.*, who observed a lower wet-etch rate (implying denser films) even with low energy ion bombardment (<20 eV) when compared with films grown without exposure to ion bombardment.[50] This also suggests that the PE-ALD of SiO_2 films at higher temperatures (>50 °C) or with higher energy ion bombardment would produce denser films.

The majority of systematic trends observed experimentally are reproduced by the model. The major trend that is not quantitatively reproduced by the model is GPC. Experimental measures of GPC for the PE-ALD of SiO_2 tend to saturate at 0.15–0.2 nm/cycle or a GPC of 0.4–0.55 layers/cycle, depending on the precursor. Our simulations for saturated GPC are up to a factor of 2 higher. This discrepancy is, in part, due to the finite resolution of our numerical mesh. However, more importantly, it may be due to an underestimation of the steric hindrance represented by surface roughness and the size of the precursor. In this simulation, precursors can attach to open sites that are bounded by a single vacancy, whereas this is likely less probable for larger precursor molecules. The extent of the steric hindrance of precursors in the model is limited to neighboring sites. In practice, the steric hindrance of large precursor molecules may extend beyond neighboring sites.

The ability to deposit PE-ALD SiO_2 films having smooth surfaces, low porosity, and proper stoichiometry is highly dependent on operating in a fully saturated mode. Achieving this goal becomes more challenging in HAR features, but this can indeed be achieved given the proper dosing and plasma exposure fluences. An additional correlation of impurity concentration (here resulting from codeposition) with roughness and porosity has also been made in these studies. One measure of success of precursors that enable low-temperature PE-ALD is likely the ability to reduce or eliminate codeposition that would otherwise lead to high impurity levels.

ACKNOWLEDGEMENTS

This work was supported by Lam Research Corporation, Samsung Electronics Co. Inc., and the National Science Foundation (PHY-2009219).

APPENDIX: SURFACE REACTION MECHANISM FOR THE PE-ALD OF SiO_2

Gas phase and surface species (Table I). Reaction mechanism: gas phase and surface species (Table II).

TABLE I. Gas-phase and surface species.

Gas-phase species	
Ions, excited states, hot neutrals, and thermal partners[a]	Ar^+, Ar_2^+, Ar(h), Ar O_2^+, O_2(h), O_2 O^+, O(h), O O_2^*, O_2 O^*, O O_3
Precursor[b]	SiH_2R_2
Sputtered materials and deposition by-products	SiH_2, SiH, Si, OH, R, HR, H_2O
Surface sites[c]	
Silicon layer	SiH_2(s), SiH(s), Si(s) O_2(s), O(s), OH–Si–OH(s), OH–
Oxygen layer	Si–H(s), OH–Si(s), O–Si–H(s)

[a] O_2^* denotes $O_2(a^1\Delta_g)$ and $O_2(b^1\Sigma_g^+)$. O^* denotes $O(^1D)$ and $O(^1S)$.
[b] R represents the ligand group from the silicon precursor. In the case of BTBAS, R denotes $[NH(C_4H_9)]$.
[c] SiO_2 is represented by a Si(s) voxel connected to two O_2(s) voxels. Ideally, SiO_2 film consists of staggered layers of Si(s) (silicon layer) and O_2(s) (oxygen layer). x–Si–y(s) represents two sites connected to Si(s) with this Si (s) not included in this voxel.

TABLE II. Reaction mechanism: gas-phase and surface species.

Reactions[a]	p_0[b]	E_{th} (eV)[b]	E_r (eV)[b]	Notes
Initial deposition of SiH_2R_2				
$W(s) + SiH_2R_2 \rightarrow W(s) + SiH_2(s) + 2HR$	0.01			c
SiH_2R_2 *deposition on a hydroxyl-rich surface*				
$OH–Si–OH(s) + SiH_2R_2 \rightarrow O_2(s) + SiH_2(s) + 2HR$	0.01			
$OH–Si–H(s) + SiH_2R_2 \rightarrow O(s) + SiH_2(s) + 2HR$	0.01			
$OH–Si(s) + SiH_2R_2 \rightarrow O(s) + SiH_2(s) + HR$	0.005			d
$O–Si–H(s) + SiH_2R_2 \rightarrow O(s) + SiH_2(s) + HR$	0.005			d
$OH–Si–O(s) + SiH_2R_2 \rightarrow O_2(s) + SiH_2(s) + HR$	0.005			d
Oxidation of surface sites				
$SiH_2(s) + O \rightarrow Si(s) + OH–Si–H(s)$	0.01			
$SiH_2(s) + O^* \rightarrow Si(s) + OH–Si–H(s)$	0.015			
$SiH_2(s) + O_3 \rightarrow Si(s) + OH–Si–H(s) + O_2$	0.015			
$SiH_2(s) + O^+ \rightarrow Si(s) + OH–Si–H(s)$	0.015			
$SiH_2(s) + O_2^* \rightarrow Si(s) + OH–Si–OH(s)$	0.015			
$SiH_2(s) + O_2^+ \rightarrow Si(s) + OH–Si–OH(s)$	0.015			
$SiH(s) + O \rightarrow Si(s) + O–Si–H(s)$	0.015			
$SiH(s) + O \rightarrow Si(s) + OH–Si(s)$	0.01			
$SiH(s) + O^* \rightarrow Si(s) + O–Si–H(s)$	0.02			
$SiH(s) + O^* \rightarrow Si(s) + OH–Si(s)$	0.015			
$SiH(s) + O_3 \rightarrow Si(s) + O–Si–H(s) + O_2$	0.02			
$SiH(s) + O_3 \rightarrow Si(s) + OH–Si(s) + O_2$	0.015			
$SiH(s) + O^+ \rightarrow Si(s) + O–Si–H(s)$	0.02			
$SiH(s) + O^+ \rightarrow Si(s) + OH–Si(s)$	0.015			
$SiH(s) + O_2^* \rightarrow Si(s) + OH–Si–O(s)$	0.02			
$SiH(s) + O_2^+ \rightarrow Si(s) + OH–Si–O(s)$	0.02			
$SiH(s) + OH \rightarrow Si(s) + OH–Si–H(s)$	0.02			
$OH–Si–H(s) + O \rightarrow OH–Si–OH(s)$	0.01			
$OH–Si–H(s) + O^* \rightarrow OH–Si–OH(s)$	0.015			
$OH–Si–H(s) + O_3 \rightarrow OH–Si–OH(s) + O_2$	0.015			
$OH–Si–H(s) + O^+ \rightarrow OH–Si–OH(s)$	0.02			
$Si(s) + O \rightarrow Si(s) + O(s)$	10^{-4}			e
$Si(s) + O^* \rightarrow Si(s) + O(s)$	2×10^{-4}			e
$Si(s) + O_3 \rightarrow Si(s) + O(s) + O_2$	2×10^{-4}			e
$Si(s) + O^+ \rightarrow Si(s) + O(s)$	2×10^{-4}			e
$Si(s) + O_2^* \rightarrow Si(s) + O_2(s)$	2×10^{-4}			e
$Si(s) + O_2^+ \rightarrow Si(s) + O_2(s)$	2×10^{-4}			e
$Si(s) + OH \rightarrow Si(s) + OH–Si(s)$	0.001			
$O(s) + O \rightarrow O_2(s)$	0.01			
$O(s) + O^* \rightarrow O_2(s)$	0.015			
$O(s) + O_3 \rightarrow O_2(s) + O_2$	0.015			
$O(s) + O^+ \rightarrow O_2(s)$	0.015			
$O(s) + O_2^* \rightarrow O_2(s) + O$	0.001			
$O(s) + O_2^+ \rightarrow O_2(s) + O(h)$	0.005			
$O(s) + OH \rightarrow OH–Si–O(s)$	0.03			
$OH–Si(s) + O \rightarrow OH–Si–O(s)$	0.015			
$OH–Si(s) + O^* \rightarrow OH–Si–O(s)$	0.02			
$OH–Si(s) + O_3 \rightarrow OH–Si–O(s) + O_2$	0.02			
$OH–Si(s) + O^+ \rightarrow OH–Si–O(s)$	0.02			
$OH–Si(s) + O_2^* \rightarrow OH–Si–O(s) + O$	0.001			
$OH–Si(s) + O_2^+ \rightarrow OH–Si–O(s) + O(h)$	0.005			

TABLE II. (*Continued.*)

Reactions[a]	p_0[b]	E_{th} (eV)[b]	E_r (eV)[b]	Notes
OH–Si(s) + OH → OH–Si–OH(s)	0.03			
O–Si–H(s) + O → OH–Si–O(s)	0.01			
O–Si–H(s) + O* → OH–Si–O(s)	0.015			
O–Si–H(s) + O_3 → OH–Si–O(s) + O_2	0.015			
O–Si–H(s) + O^+ → OH–Si–O(s)	0.015			
Sputtering by ion and hot neutrals				
SiH_2(s) + I^+ → SiH_2 + I(h)	0.9	35	140	f
SiH(s) + I^+ → SiH + I(h)	0.9	35	140	f
Si(s) + I^+ → Si + I(h)	0.9	35	140	f
OH–Si–OH(s) + I^+ → OH–Si(s) + OH + I(h)	0.9	30	120	f
OH–Si–H(s) + I^+ → OH + H + I(h)	0.9	30	120	f,g
O–Si–H(s) + I^+ → O + H + I(h)	0.9	30	120	f,g
OH–Si(s) + I^+ → OH + I(h)	0.9	30	120	f
OH–Si–O(s) + I^+ → OH–Si(s) + O + I(h)	0.45	30	120	f
OH–Si–O(s) + I^+ → O(s) + OH + I(h)	0.45	30	120	f
O(s) + I^+ → O + I(h)	0.9	30	120	f
O_2(s) + I^+ → O(s) + O + I(h)	0.9	30	120	f
R(s) + I^+ → R + I(h)	0.9	40	160	f
R(s) *removal by reactive oxygen species*				
R(s) + O → O(s) + R	10^{-5}			
R(s) + O* → O(s) + R	10^{-4}			
R(s) + O_3 → O(s) + R + O_2	10^{-6}			
Redeposition of sputtered species				
SiH(s) + SiH_2 → SiH(s) + SiH_2(s)	0.03			
SiH(s) + SiH → SiH(s) + SiH(s)	0.03			
SiH(s) + Si → SiH(s) + Si(s)	0.03			
SiH(s) + R → SiH(s) + R(s)	0.01			
Si(s) + SiH_2 → Si(s) + SiH_2(s)	0.001			e
Si(s) + SiH → Si(s) + SiH(s)	0.001			e
Si(s) + Si → Si(s) + Si(s)	0.001			e
Si(s) + R → Si(s) + R(s)	0.001			e
O(s) + SiH_2 → O(s) + SiH_2(s)	0.03			
O(s) + SiH → O(s) + SiH(s)	0.03			
O(s) + Si → O(s) + Si(s)	0.03			
O(s) + R → O(s) + R(s)	0.01			
O_2(s) + SiH_2 → O_2(s) + SiH_2(s)	0.03			
O_2(s) + SiH → O_2(s) + SiH(s)	0.03			
O_2(s) + Si → O_2(s) + Si(s)	0.03			
O_2(s) + R → O_2(s) + R(s)	0.01			
OH–Si(s) + SiH_2 → OH–Si(s) + SiH_2(s)	0.03			
OH–Si(s) + SiH → OH–Si(s) + SiH(s)	0.03			
OH–Si(s) + Si → OH–Si(s) + Si(s)	0.03			
O–Si–H(s) + SiH_2 → O–Si–H(s) + SiH_2(s)	0.03			
O–Si–H(s) + SiH → O–Si–H(s) + SiH(s)	0.03			
O–Si–H(s) + Si → O–Si–H(s) + Si (s)	0.03			
OH–Si–O(s) + SiH_2 → OH–Si–O(s) + SiH_2(s)	0.03			
OH–Si–O(s) + SiH → OH–Si–O(s) + SiH(s)	0.03			
OH–Si–O(s) + Si → OH–Si–O(s) + Si(s)	0.03			
OH–Si–O(s) + R → OH–Si–O(s) + R(s)	0.01			

TABLE II. (*Continued.*)

Reactions[a]	p_0[b]	E_{th} (eV)[b]	E_r (eV)[b]	Notes
Oxidation by hydroxyl radical				
$SiH_2(s) + OH \rightarrow SiH(s) + H_2O$	0.01			
$SiH(s) + OH \rightarrow Si(s) + H_2O$	0.01			
$OH–Si–OH(s) + OH \rightarrow OH–Si–O(s) + H_2O$	0.01			
$OH–Si–H(s) + OH \rightarrow O–Si–H(s) + H_2O$	0.01			
$OH–Si–H(s) + OH \rightarrow OH–Si(s) + H_2O$	0.01			
$O–Si–H(s) + OH \rightarrow O(s) + H_2O$	0.01			
$OH–Si–O(s) + OH \rightarrow O_2(s) + H_2O$	0.01			
Recombination by the sputtered ligand group				
$SiH_2(s) + R \rightarrow SiH(s) + HR$	0.01			
$SiH(s) + R \rightarrow Si(s) + HR$	0.01			
$OH–Si–OH(s) + R \rightarrow OH–Si–O(s) + HR$	0.01			
$OH–Si–H(s) + R \rightarrow O–Si–H(s) + HR$	0.01			
$OH–Si–H(s) + R \rightarrow OH–Si(s) + HR$	0.01			
$O–Si–H(s) + R \rightarrow O(s) + HR$	0.01			
Oxygen recombination				
$O(s) + O \rightarrow O_2$	6×10^{-5}			Reference 33
$O(s) + O^* \rightarrow O_2$	10^{-4}			
$O(s) + O_3 \rightarrow O_2 + O_2$	10^{-4}			
$O(s) + O^+ \rightarrow O_2$	10^{-4}			
$O_2(s) + O \rightarrow O(s) + O_2$	6×10^{-5}			Reference 33
$O_2(s) + O^* \rightarrow O(s) + O_2$	10^{-4}			
$O_2(s) + O_3 \rightarrow O(s) + O_2 + O_2$	10^{-4}			
$O_2(s) + O^+ \rightarrow O(s) + O_2$	10^{-4}			
$O–Si–H(s) + O \rightarrow O_2 + H$	6×10^{-5}			Reference 33,g
$O–Si–H(s) + O^* \rightarrow O_2 + H$	10^{-4}			g
$O–Si–H(s) + O_3 \rightarrow O_2 + O_2 + H$	10^{-4}			g
$O–Si–H(s) + O^+ \rightarrow O_2 + H$	10^{-4}			g
$OH–Si–O(s) + O \rightarrow OH–Si(s) + O_2$	6×10^{-5}			Reference 33
$OH–Si–O(s) + O^* \rightarrow OH–Si(s) + O_2$	10^{-4}			
$OH–Si–O(s) + O_3 \rightarrow OH–Si(s) + O_2 + O_2$	10^{-4}			
$OH–Si–O(s) + O^+ \rightarrow OH–Si(s) + O_2$	10^{-4}			
Dissociation of O_3				
$Surface(s) + O_3 \rightarrow Surface(s) + O + O_2$	0.05			h

[a]All ions neutralize on surfaces, returning to gas phase as their hot neutral partner. Ions and their hot neutral partners undergo the same surface reactions with the same probability. Only surface reactions for ions are shown in the table. All such reactions (with the exception of neutralization) should be duplicated for the ions' hot neutral partner. Ar_2^+ is reflected from the surface as two Ar hot neutrals.

[b]If E_{th} and E_r are blank, the reaction has no energy dependence and the probability of the reaction is a constant, p_0. If E_{th} and E_r have nonzero values, the reaction has an energy-dependent probability. When the probability of reaction is less than unity, the remaining probability is allocated to a nonreacting reflection from the surface.

[c]W(s) is the ideal surface upon which the SiO_2 PE-ALD is performed with sufficient hydroxyl sites for the first-step silicon precursor dosing.

[d]The ligand group remnants R(s) during precursor dosing are addressed using a codeposition probability. R(s) voxels are deposited with the silicon with a deposition probability p_R.

[e]Oxidation probability of Si(s) is reduced to avoid excessive oxidation when more than one surface of the Si(s) voxel is exposed to the plasma. The adjustment is made only for Si(s) as it is the final product upon which a high-density reactant (O) can be deposited.

[f]Reaction with physical sputtering angular dependence.

[g]The hydrogen site is removed along with the oxygen or hydroxyl sites in a sputtering and oxygen recombination process due to the lack of information about the neighbors of the direct surface reactant. This has a minor effect in the current work due to the low concentrations of OH–Si–H(s) and O–Si–H(s) (<1%) and low etching probability.

[h]Surface(s) represents any solid-state surface site.

DATA AVAILABILITY

The data that support the findings of this study are available from the corresponding author upon reasonable request.

REFERENCES

[1]V. Cremers, R. L. Puurunen, and J. Dendooven, Appl. Phys. Rev. **6**, 021302 (2019).
[2]A. J. M. Mackus, A. A. Bol, and W. M. M. Kessels, Nanoscale **6**, 10941 (2014).
[3]H. V. Bui, F. Grillo, and J. R. van Ommen, Chem. Commun. **53**, 45 (2017).
[4]A. Sharma *et al.*, Nanotechnology **31**, 255603 (2020).
[5]R. W. Johnson, A. Hultqvist, and S. F. Bent, Mater. Today **17**, 236 (2014).
[6]R. A. Ovanesyan, E. A. Filatova, S. D. Elliott, D. M. Hausmann, D. C. Smith, and S. Agarwal, J. Vac. Sci. Technol. A **37**, 060904 (2019).
[7]H. B. Profijt, S. E. Potts, M. C. M. van de Sanden, and W. M. M. Kessels, J. Vac. Sci. Technol. A **29**, 050801 (2011).
[8]J. R. Bakke, K. L. Pickrahn, T. P. Brennan, and S. F. Bent, Nanoscale **3**, 3482 (2011).
[9]C.-C. Chao, J. S. Park, X. Tian, J. H. Shim, T. M. Gür, and F. B. Prinz, ACS Nano **7**, 2186 (2013).
[10]A. Kobayashi, N. Tsuji, A. Fukazawa, and N. Kobayashi, Thin Solid Films **520**, 3994 (2012).
[11]C. A. Murray, S. D. Elliott, D. Hausmann, J. Henri, and A. LaVoie, ACS Appl. Mater. Interfaces **6**, 10534 (2014).
[12]D. Shin, H. Song, M. Lee, H. Park, and D.-H. Ko, Thin Solid Films **660**, 572 (2018).
[13]F. Koehler, D. H. Triyoso, I. Hussain, B. Antonioli, and K. Hempel, Phys. Status Solidi C **11**, 73 (2014).
[14]T. Usui, C. A. Donnelly, M. Logar, R. Sinclair, J. Schoonman, and F. B. Prinz, Acta Mater. **61**, 7660 (2013).
[15]K.-M. Jeon, J.-S. Shin, J.-Y. Yun, S. J. Lee, and S.-W. Kang, J. Vac. Sci. Technol. A **32**, 031511 (2014).
[16]H. Jung, W.-H. Kim, I.-K. Oh, C.-W. Lee, C. Lansalot-Matras, S. J. Lee, J.-M. Myoung, H.-B.-R. Lee, and H. Kim, J. Mater. Sci. **51**, 5082 (2016).
[17]Y. Civale *et al.*, "Highly conformal plasma-enhanced atomic-layer deposition silicon dioxide liner for high aspect-ratio through-silicon via 3D interconnections," 2012 4th Electronic System Integration Technology Conference 2012, pp. 1–4.
[18]J. M. Chan, X. Cheng, K. C. Lee, W. Kanert, and C. S. Tan, "Reliability evaluation of copper (Cu) through-silicon vias (TSV) barrier and dielectric liner by electrical characterization and physical failure analysis (PFA)," 2017 IEEE 67th Electronic Components and Technology Conference (ECTC) 2017, pp. 73–79.
[19]K. Endo, Y. Ishikawa, T. Matsukawa, Y. Liu, S.-i. O'uchi, K. Sakamoto, J. Tsukada, H. Yamauchi, and M. Masahara, Solid State Electron. **74**, 13 (2012).
[20]F. Palumbo, C. Wen, S. Lombardo, S. Pazos, F. Aguirre, M. Eizenberg, F. Hui, and M. Lanza, Adv. Funct. Mater. **30**, 1900657 (2020).
[21]J. H. Stathis, IBM J. Res. Dev. **46**, 265 (2002).
[22]O. Sneh, M. L. Wise, A. W. Ott, L. A. Okada, and S. M. George, Surf. Sci. **334**, 135 (1995).
[23]S.-W. Lee, K. Park, B. Han, S.-H. Son, S.-K. Rha, C.-O. Park, and W.-J. Lee, Electrochem. Solid State Lett. **11**, G23 (2008).
[24]G.-Y. Fang, L.-N. Xu, Y.-Q. Cao, L.-G. Wang, D. Wu, and A.-D. Li, Chem. Commun. **51**, 1341 (2015).
[25]Y.-J. Choi, S.-M. Bae, J.-H. Kim, E.-H. Kim, H.-S. Hwang, J.-W. Park, H. Yang, E. Choi, and J.-H. Hwang, Ceram. Int. **44**, 1556 (2018).
[26]M. Putkonen *et al.*, Thin Solid Films **558**, 93 (2014).
[27]A. Mallikarjunan, H. Chandra, M. Xiao, X. Lei, R. M. Pearlstein, H. R. Bowen, M. L. O'Neill, A. Derecskei-Kovacs, and B. Han, J. Vac. Sci. Technol. A **33**, 01A137 (2015).
[28]M. J. Kushner, J. Phys. D: Appl. Phys. **42**, 194013 (2009).
[29]Y. Zhang, C. Huard, S. Sriraman, J. Belen, A. Peterson, and M. J. Kushner, J. Vac. Sci. Technol. A **35**, 021303 (2017).
[30]S. Huang, V. Volynets, J. R. Hamilton, S. Lee, I.-C. Song, S. Lu, J. Tennyson, and M. J. Kushner, J. Vac. Technol. A **35**, 031302 (2017).
[31]C. C. Cheng, K. V. Guinn, V. M. Donnelly, and I. P. Herman, J. Vac. Sci. Technol. A **12**, 2630 (1994).
[32]C. F. Abrams and D. B. Graves, J. Appl. Phys. **86**, 2263 (1999).
[33]K. Arts, M. Utriainen, R. L. Puurunen, W. M. M. Kessels, and H. C. M. Knoops, J. Phys. Chem. C **123**, 27030 (2019).
[34]Y. Lu, A. Kobayashi, H. Kondo, K. Ishikawa, M. Sekine, and M. Hori, Jpn. J. Appl. Phys. **53**, 010305 (2014).
[35]S. E. Potts, H. B. Profijt, R. Roelofs, and W. M. M. Kessels, Chem. Vap. Deposition **19**, 125 (2013).
[36]G. Dingemans, C. A. A. van Helvoirt, D. Pierreux, W. Keuning, and W. M. M. Kessels, J. Electrochem. Soc. **159**, H277 (2012).
[37]H. Li *et al.*, Jpn. J. Appl. Phys. **59**, SJJA01 (2020).
[38]H. C. M. Knoops, T. Faraz, K. Arts, and W. M. M. Kessels, J. Vac. Sci. Technol. A **37**, 030902 (2019).
[39]K.-M. Jeon, J.-S. Shin, J.-Y. Yun, S. J. Lee, and Sang-Woo Kang, J. Vac. Sci. Technol. A **32**, 031511 (2014).
[40]H. Kim *et al.*, J. Vac. Sci. Technol. A **33**, 01A146 (2015).
[41]Y.-S. Lee, J.-H. Han, J.-S. Park, and J. Park, J. Vac. Sci. Technol. A **35**, 041508 (2017).
[42]H.-P. Ma *et al.*, Nanomaterials **9**, 55 (2019).
[43]Z. Zhu, P. Sippola, O. M. E. Ylivaara, C. Modanese, M. D. Sabatino, K. Mizohata, S. Merdes, H. Lipsanen, and H. Savin, Nanoscale Res. Lett. **14**, 55 (2019).
[44]Z. Zhu, P. Sippolla, H. Lipsanen, H. Savin, and S. Merdes, Jpn. J. Appl. Phys. **57**, 125502 (2018).
[45]Y. Lee, S. Seo, I.-K. Oh, S. Lee, and H. Kim, Ceram. Int. **45**, 17662 (2019).
[46]K. Arts, S. Deijkers, R. L. Puurunen, W. M. M. Kessels, and H. C. M. Knoops, J. Phys. Chem. C **125**, 8244 (2021).
[47]M. R. Baklanov *et al.*, Appl. Phys. Rev. **6**, 011301 (2019).
[48]R. Tatsumi, S. Fukuda, and S. Kadomura, Jpn. J. Appl. Phys. **33**, 2175 (1994).
[49]V. Beladiya *et al.*, Nanoscale **12**, 2089 (2020).
[50]K. Arts, J. H. Deijkers, T. Faraz, R. L. Puurunen, W. M. M. Kessels, and H. C. M. Knoops, Appl. Phys. Lett. **117**, 031602 (2020).